The Role of CCR7 and its Atypical Chemokine Receptor, CCRL1, in Lymph Node Metastasis

AND

Does Rad6 Alter p53 Function Via Pituitary Tumour Transforming Gene 1 (PTTG1) – Binding Factor (PBF)?

By
Bhavika Modasia

A thesis submitted to the University of Birmingham for the degree of MASTER OF RESEARCH

UNIVERSITY OF BIRMINGHAM

Department of Immunity and Infection
College of Medical and Dental Sciences
University of Birmingham
August 2012

wellcome trust

MAIN TABLE OF CONTENTS

PROJECT 1:

PROJECT 2:

The Role of CCR7 and its Atypical Chemokine Receptor, CCRL1, in Lymph Node Metastasis

By

Bhavika Modasia

13th August 2012

UNIVERSITY OF BIRMINGHAM

wellcome trust

ABSTRACT

Background: Metastasis is a highly complex process and the detailed molecular mechanisms are not fully understood. In recent years, a role for chemokine receptors in tumour growth and metastasis has emerged. CCR7 is involved in the regulation of leukocyte homing to regional lymph nodes. Interestingly, invasion of lymphatic vessels by tumour cells and their migration towards draining lymph nodes resembles this process. Several lines of evidence exist to implicate CCR7 in lymph node metastasis. In contrast, little is known about the contribution of CCRL1 to lymph node metastasis.

Aims: The main objective was to investigate CCR7-driven metastasis in the lymph node and to assess whether CCRL1 expression affects this process.

Methods: Tumour growth was assessed through the immunofluorescent staining of murine lymph node sections. Tumour kinetics was assessed by inoculation of WT and CCRL1-knockout mice with CCR7-expressing B16 melanoma cells.

Results: CCR7-expressing B16 melanoma establishes in the B cell areas of the lymph node and suppresses both CCRL1 and CCL21 expression in the sinus. Depletion of CCRL1 does not affect metastatic growth. However, CCRL1-knockout mice develop primary melanoma tumours with enhanced kinetics.

Discussion: These findings provide further insight into the role of chemokine receptors in melanoma metastasis.

ACKNOWLEDGMENTS

I would like to thank my supervisor Professor Antal Rot, for offering me the opportunity to carry out my project in his lab and for the support and encouragement. I would also like to thank everyone in the group. In particular Maria Ulvmar, for her endless support, encouragement and patience. I am truly grateful. I would also like to thank Poonam Kelay Jakhu, Sarah Cook and Beth Lucas for the lab banter and for making me feel so welcome!

TABLE OF CONTENTS

LIST OF ILLUSTRATIONS

ABBREVIATIONS

ACR – Atypical Chemokine Receptor

APC – Antigen Presenting Cell

CCL – CC-chemokine Ligand

CCRL1 – CC-chemokine Receptor Like 1

CCX-CKR – Chemocentryx Chemokine Receptor (CCRL1)

CD – Cluster of Differentiation

CTL – cytotoxic T cell

DARC – Duffy Antigen Receptor for Chemokines

DC – Dendritic Cell

ELC – EBI1 Ligand Chemokine

GPCR – G-protein Coupled Receptor

HEV – High Endothelial Venule

i.p. – Intraperitoneal

Ig – Immunoglobulin

ILN – Inguinal Lymph Node

KO – knockout

LN – Lymph Node

LTi – Lymphoid Tissue Inducer

MHC – Major Histocompatibility Complex

MLN – Mesenteric Lymph Node

PBL – peripheral blood lymphocyte

plt – Paucity of Lymph Node T cells

SA – Streptavidin

SLC – Secondary Lymphoid-tissue Chemokine

SLN – Sentinel Lymph Node

T_{CM} – central memory T cell

TCZ – T cell zone

T_{Reg} – regulatory T cell

WT – wild type

1. INTRODUCTION

1.1 Cutaneous Melanoma

Cutaneous melanoma is characterised by the malignant growth of melanocytes, the melanin-producing cells of the skin. Of all forms of skin cancer, malignant melanoma remains the most fatal and is one of the most common malignancies among Caucasians (1). An estimated 47 000 cases are diagnosed every year in the United States alone (2) and the overall incidence appears to be increasing at a rate faster than for any other cancer type(3). Treatment for primary melanoma typically involves surgical excision of the tumour mass and, if treated early, is associated with a 5-year survival rate of approximately 81-93% (4).

1.1.1 Metastatic Melanoma

Metastatic melanoma is considered to be one of the most treatment-refractory cancers and is the leading cause of death from melanoma. Despite therapeutic attempts it remains virtually impossible to eradicate, with a median overall survival for patients diagnosed with metastatic melanoma of just 8-9 months (5). Until recently, very few therapies have been approved for the treatment of metastatic melanoma. Mono-chemotherapy with Dicarbazine has long been the first-line treatment for metastatic melanoma but, to date, has not been shown to improve overall survival rates (6). High-dose IL-2 is an additional FDA-approved therapy. Although administration of high-dose IL-2 can result in a durable response, this has only been the case for a very limited number of patients (6).

1.2 The Metastatic Cascade

Metastasis is a highly organised process that arises following the dissemination and growth of cancerous cells from the original site to one, or more, distal sites within the human body. The ensuing secondary tumours are responsible for approximately 90% of human cancer-related deaths(7). The process itself is exceedingly complex and comprises a series of sequential steps. The formation of new blood and lymphatic vessels via processes known as angiogenesis and lymphangiogenesis respectively is essential for the growth of the primary tumour. Moreover, they provide a means of escape for the tumour cells from primary sites, which may then colonize secondary sites.

As a result of changes in the expression of genes as well as potential epigenetic changes, the primary tumour cells undergo extensive cytoskeletal remodelling. This consequently leads to a breakdown in cell-to-cell adhesion, thus enabling the tumour cells to shed away from the primary tumour mass and to invade nearby blood vessels – known as intravasation. Alternatively, the cells may invade surrounding lymphatic vessels. Once in the circulation, surviving tumour cells will become arrested, mainly due to receptor-mediated signalling but also due to size restrictions (8). These arrested cells will then extravasate into the surrounding tissue, where they must proliferate in order to form micrometastases. On the other hand, tumour cells that enter the lymphatic vessel may settle and initiate tumour growth within the regional draining lymph node(s).

Clinical observations of cancer patients and *in vivo* experimental models have demonstrated that certain types of cancers have a tendency to form metastases in specific organs (9). For instance, malignant melanoma preferentially metastasises to the regional lymph nodes draining primary tumour sites. It has been suggested that up to 60% of melanomas cause lymph node metastases (1). Such metastases have a major

impact on patient prognosis as 75-80% of patients with lymph node involvement also exhibit distant metastases (10,11). Although much progress has been made in the field of cancer research, the detailed molecular mechanisms by which tumour cells metastasise to the lymph nodes remain elusive. There is now a growing body of evidence to support a role of chemokine receptors and their corresponding ligands in tumour growth, survival and metastasis (8).

1.3 Chemokines and Their Receptors

Chemokines represent an important superfamily of small chemotactic proteins (8-11 kDa (8)), which are further classified in to 4 subgroups (C, CC, CXC, CX3C) based upon the relative position of conserved cysteine residues located near their amino termini (12). A diverse class of cell-surface receptors, known as the seven-transmembrane domain G-protein-coupled receptors (GPCR), mediate chemokine signalling. At present, almost 50 chemokines (13) and 19 different receptors (12) have been identified. Through various chemokine-GPCR combinations, chemokines are able to evoke a number of distinct cellular responses including proliferation, differentiation and angiogenesis (8,12). Their best known function, however, is to promote the directional migration of leukocytes towards extravascular target tissues, both under steady-state ('homeostatic' chemokines) and inflammatory ('inflammatory' chemokines) conditions. Upon GPCR activation, leukocytes assume a polarised morphology, owing to the reorganisation of integrins and the actin cytoskeleton (12). These polarised cells form sheet-like lamellipodia at the leading edge and contractile acto-myosin filaments at the trailing edge, both of which drive cell locomotion (12). Chemokine receptors are also concentrated at the leading edge and thus enable unidirectional migration towards increasing chemokine gradients.

It has been well established that the arrest and firm adhesion of leukocytes to endothelial cells is also induced by chemokines (12,13). Endothelial cell-bound chemokine signalling triggers the activation and subsequent increase in affinity of the β-integrins, LFA-1 and VLA-4 present on leukocytes (14,15). These activated integrins then interact with cell adhesion molecules present on the endothelium, thus promoting leukocyte arrest and crawling (14). Current evidence suggests that apical endothelial chemokines may also participate in the transendothelial migration of previously arrested leukocytes (16).

1.3.1 Atypical Chemokine Receptors

Recently, an alternative group of chemokine receptors have emerged. These 'atypical' chemokine receptors (ACR) are heptaspanning membrane receptors and there are currently 5 family members: DARC, D6, CXCR7, CCRL1 and CCRL2. Although structurally homologous to classical chemokine receptors, they differ in that they are unable to signal along classical G-protein-mediated pathways normally activated upon chemokine binding (17). This is due to the fact that they possess (or completely lack) a modified DRYLAIV motif within the second intracellular loop (17). This canonical motif is absolutely essential for coupling to G-proteins. Nevertheless, ACRs can efficiently internalise chemokines (17,18) and, are thus perceived to play a role in the regulation of chemokine bioavailability (18) and in the generation of functional chemokine gradients (17). ACRs may influence the response to chemokines both by scavenging chemokines and targeting them for lysosomal degradation or by transporting them across physiological barriers (17-19).

1.4 CC-Chemokine Receptor 7

The chemokine receptor, CCR7 is predominantly expressed by cells of the immune system including mature DCs, naïve T and B cells, central memory T cells (T_{CM}) and regulatory T cells (T_{Reg}) (20). The homeostatic chemokines, CCL19 and CCL21, are reported to be the sole ligands for CCR7. Both chemokines appear to be constitutively expressed by fibroblastic reticular cells concentrated in the T cell areas of secondary lymphoid organs, such as the thymus, spleen and lymph nodes (20). In particular, CCL19 is expressed on the lumen of HEVs, the principal route of entry into the lymph node for lymphocytes, and CCL21 by the afferent lymphatic endothelium (20). Only in mice is CCL21 present on the luminal side of HEVs (20).

1.4.1 Lymph Node Architecture

The lymph node is an encapsulated organ that is composed of two histologically distinct regions – the cortex and the medulla (Figure 1.1). The cortex is further subdivided into the paracortex, which mainly consists of T cells, and the outer cortex, which is composed of primary B cell follicles and is the main site of germinal centre formation (21). The medulla, on the other hand, comprises a dense network of medullary sinuses that are separated by medullary cords containing plasma cells, macrophages and T cells (21).

Lymph enters the lymph node via a series of afferent lymphatic vessels. This lymph flows through to the subcapsular sinus and then drains to trabecular sinuses (21). The lymph then filters through the LN and eventually collects in the medullary sinuses (21). These medullary sinuses converge at the hilum to form the efferent lymphatic vessel, which carries lymph away from the lymph node (21).

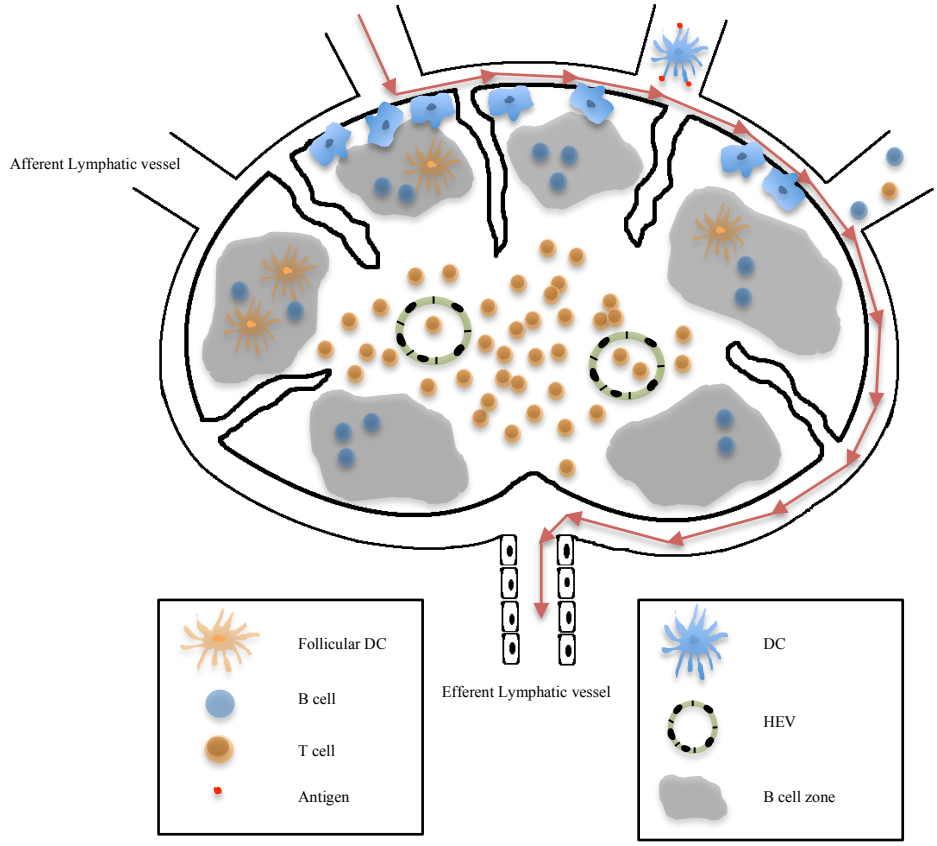

Figure 1.1: The Structure of the Lymph Node

The afferent lymphatic vessels carry lymph into the subcapsular sinus. Macrophages sample the lymph for pathogens for presentation to B cells. The lymph then drains into trabecular sinuses lined by fibroblastic reticular cells. Chemokines are also transported in these sinuses to HEV to attract lymphocytes. The lymph eventually collects in the medullary sinuses, which converge at the hilum, forming the efferent lymphatic vessel.

The Role of CCR7 in Lymph Node Homing and Positioning

In recent years, a number of lymphoid chemokine receptors (and corresponding ligands) have emerged that regulate the homing of leukocytes to lymph nodes. Immature DCs in the skin constantly patrol the tissue in search for antigen, which they process and present via MHC. Upon exposure to inflammatory cytokines, the DCs undergo maturation and downregulate the expression of inflammatory chemokine receptors, whilst concomitantly upregulating CCR7 (22). This upregulation is absolutely essential for the directed migration of DCs from the dermis toward CCL21-expressing afferent lymphatics (15,22,23). Similarly, entry of lymphocytes into the

lymphatics is also dependent on CCR7 and its cognate ligands (20,23). The number of T cells present in the LNs of CCR7-deficient mice is markedly reduced (20). Likewise, CCR7-deficient DCs display a strong reduction in their ability to enter dermal lymphatic vessels (23).

CCR7 also plays a crucial role in the firm arrest and subsequent transmigration of leukocytes across the afferent lymph vessels (DCs) or HEVs (T cells) into the draining LN. Using TNFα-activated Human Umbilical Vein Endothelial Cells (HUVEC) as an *in vitro* model of inflamed endothelium, Cinamon *et al* were able to demonstrate that adsorption of CXCL12 or CCL19 on the apical surface of HUVECs induced significant arrest of peripheral blood lymphocytes (PBL) (16). In addition, approximately 70% of the arrested lymphocytes were able to successfully transmigrate across the endothelium (16). Comparatively fewer lymphocytes could transmigrate in the absence of immobilised chemokines (16). In DCs, neutralisation of CCL21 effectively blocked transendothelial migration and was associated with a lack of β_2 integrin activation (15).

It is also widely accepted that CCR7 signals contribute to the proper positioning of immune cells and the generation of functional microenvironments within secondary lymphoid organs. Naïve T cells constantly circulate through secondary lymphoid organs in search for DCs bearing their cognate antigen. Activated DCs, under the influence of CCL19/21 expressed by HEV, traverse the subcapsular sinus and are guided into the deep paracortical T cell zone (TCZ) (23). This process is of great importance as it increases the likelihood of naïve T cells encountering their cognate DC. Indeed, CCR7-deficient DCs fail to penetrate the TCZ and remain 'trapped' in the subcapsular sinus (23). Such defects in immune cell homing have been linked with impaired immunity and tolerance (20). Signalling through CCR7 has also been

reported to control the positioning of follicular B cells at the T cell border, thus enabling T cell – B cell interactions (20).

1.5 CCRL1: Chemocentryx Chemokine Receptor

CCRL1 (also known as CCX-CKR1, CCR10 and CCR11) is a relatively new member of the ACR superfamily and although studied to a lesser extent, is known to be the only ACR that binds with high affinity to homeostatic chemokines, namely CCL19, CCL21 and CCL25 (17). As with all other ACRs, CCRL1 is incapable of initiating downstream signalling events that mediate physiological processes, such as chemotaxis and its exact function is largely unknown. CCRL1 expression has been documented specifically in epidermal cells, thymic epithelial cells and stromal cells that line the LN marginal sinus (24).

The discovery that CCRL1 is able to bind the same ligands as CCR7 has led to the proposal that CCRL1 may function as a chemokine scavenger and may thus affect chemokine bioavailability and subsequent CCR7-mediated chemotactic responses (18). Stable transfection of HEK293 cells has demonstrated that upon chemokine exposure, both CCR7 and CCRL1 rapidly internalise CCL19. In CCRL1 expressing cells this also leads to very efficient lysosomal degradation (18). Further internalisation of CCL19 through CCRL1 unlike CCR7, does not result in receptor desensitisation but rather leads to enhanced chemokine sequestration (18). In support of this, mice lacking CCRL1 display significant increases in the levels of CCL19 and CCL21 within peripheral LNs and in the blood (19). Despite the abundance of CCR7-ligands, CCRL1-deficient mice appear to have decreased lymph node cellularity (19) and display gross abnormalities in steady-state homing of $CD11c^{+}MHCII^{high}$ DCs (24). This may result from receptor desensitisation due to increased levels of CCL19 and CCL21 or may be due to the inability to establish pro-migratory chemokine gradients

(17,18). CCRL1 has also been implicated in the differentiation of $CD4^+$ T cells *in vivo* (19).

1.6 The Role of CCR7 and its Atypical Chemokine Receptor in Lymph Node Metastasis

As previously mentioned, the regional draining LNs represent the most common site of metastasis for melanoma and the occurrence of such metastases is strongly correlated with poor patient outcome (8). Interestingly, the invasion of lymphatic vessels by tumour cells and their subsequent migration to the SLN bears striking similarities with the normal trafficking of antigen-bearing DCs from the skin to secondary lymphoid organs during the course of inflammation. Considering that the emigration of DCs to regional draining LNs is under the control of CCR7 and its ligands, it is likely that CCR7 may also be implicated in lymph node metastasis (Figure 1.2).

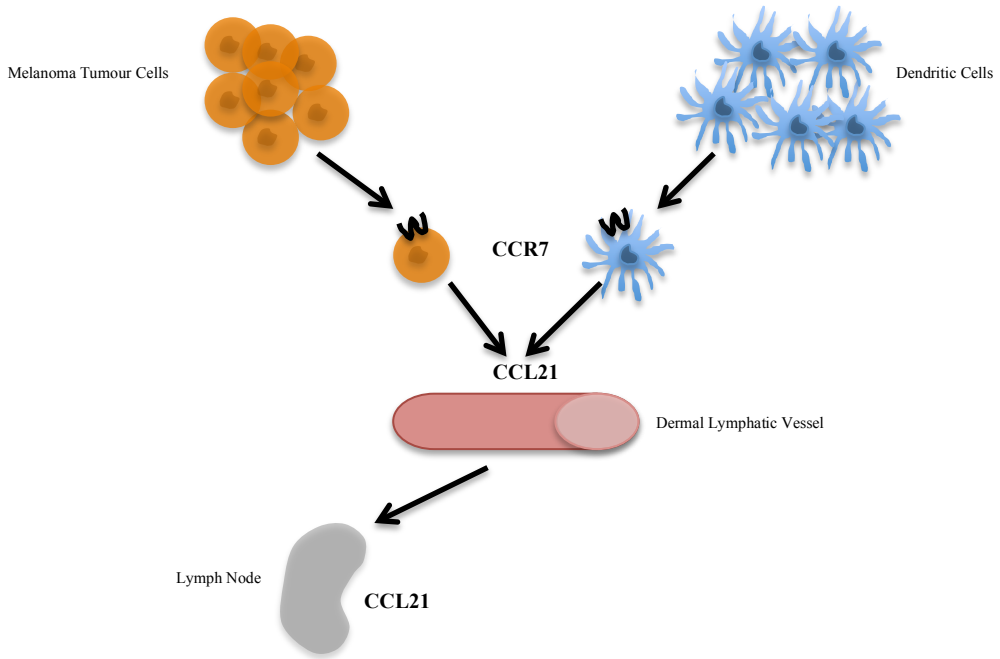

Figure 1.2: Melanoma Metastasis Resembles Immune Cell Homing to Lymph Nodes

Activated DCs in the periphery undergo maturation and downregulate the expression of inflammatory cytokines, whilst concomitantly upregulating CCR7. The upregulated expression of CCR7 enables DCs to respond chemotactically to CCL21 expressed by dermal lymphatic vessels. The DCs then flow to the regional lymph node, which is rich in CCL21. Likewise, melanoma tumour cells expressing CCR7 may invade afferent lymphatic vessels more efficiently and be retained in regional lymph nodes.

This is supported by clinical findings indicating that CCR7 is expressed by a number of tumour types including breast, cervix, head and neck, and melanoma (25-27). Furthermore, overexpression of CCR7 in B16 murine melanoma cells has been demonstrated to result in an approximate 700-fold increase in lymph node metastasis - an observation that is effectively blocked using a neutralising anti-CCL21 antibody (1,10). In accord with these findings, lymphatic endothelial cells express CCL21, which has been shown to stimulate the directed migration of malignant melanoma cells towards the lymphatics (11). Recent data also indicates that CCR7 expression may be involved in lymphangiogenesis and anti-tumour immunity as the expression of the lymphatic marker, podoplanin, appears to be upregulated in CCR7-expressing B16

melanoma tumours, whilst the expression of interferon-γ-associated genes and MHC class I and II appear to be markedly reduced (28).

The role of CCR7 in cancer progression is clearly well established and there is now evidence to implicate CCRL1 in tumourigenesis and metastasis. A significant correlation has been reported between CCRL1 expression and lymph node metastasis in human breast cancer, with lower levels of expression being associated with poorer prognosis (29). These results raise a number of questions and it will be interesting to see how CCRL1 expression affects the axis role of CCR7-CCL19/21 in nodal metastasis.

2. MATERIALS AND METHODS

2.1 Materials

Cell Lines

- B16-F1 murine melanoma cell line obtained from ATCC (♯CRL-6323)
- CCR7-transfected B16-F1 melanoma cell line obtained from Professor Sam T Hwang (1)

Cell Culture

- Dulbecco's Modified Eagle Medium (DMEM) – Sigma-Aldrich, UK
- RPMI 1640 (- L-Glutamine) – Sigma-Aldrich, UK

Antibodies

- Rat eFluor® 450 conjugated anti-mouse/human CD45R (B220) – eBioscience ♯48-0452-82
- FITC-conjugated anti-mouse CD45.2 – eBioscience ♯11-0454-85
- Rabbit polyclonal antibody to TRP2 – Abcam ♯Ab74073
- Polyclonal goat anti-rabbit IgG biotinylated – Dako ♯E0432
- Rabbit polyclonal antibody to Lyve-1 – Abcam ♯Ab14917
- Alexa Fluor® 555 donkey anti-rabbit IgG (H+L) – Invitrogen ♯A31572
- Anti-mouse Lyve-1 eFluor® 660 – eBioscience ♯50-0443-82
- Goat anti-mouse CCL21 – R&D Systems
- CCXCKR (C-16) goat polyclonal IgG (CCRL1) – Santa Cruz Biotechnology ♯ SC-46835
- Alexa Fluor® 647 donkey anti-goat IgG (H+L) – Invitrogen ♯A21447

- Alexa Fluor® 488 donkey anti-rat IgG (H+L) – Invitrogen ♯A11006
- Langerin/CD207 monoclonal antibody – Dendtritics ♯DDX0362
- Anti-mouse CCR7-PE conjugated IgG – eBioscience ♯12-1971-82
- Anti-mouse CD16/32 purified IgG (Fc block) – eBioscience ♯14-0161-85
- Purified rat anti-mouse CD31 – BD Pharmingen ♯550274
- Anti-mouse CD11b eFluor® 450 – eBioscience ♯48-0112-82
- Anti-mouse CD11c-FITC – eBioscience ♯11-0114-82
- Anti-FITC/Oregon green rabbit IgG fraction Alexa Fluor® 488 conjugate – Invitrogen ♯A11090
- Biotin conjugated anti-mouse CD3e – eBioscience ♯13-0033-85
- Rat anti-mouse CD4-647 – eBioscience ♯14-0043-81. Conjugated in-house by Dr. David Withers.
- eFluor® 660 conjugated anti-mouse CD8 (alpha subunit, CD8a, Ly-2) – eBioscience ♯50-0087-82
- Anti-mouse/rat Foxp3-FITC – eBioscience ♯50-0087-82
- Goat anti-rat FITC – Southern Biotech ♯3030-02
- Goat anti-rabbit FITC – Southern Biotech ♯4050-02
- Alexa Fluor® 488 donkey anti-rat IgG (H+L) – Invitrogen ♯A21208

Primers

- 11com5 primer – obtained from Professor Robert Nibbs (19)
- 3IRES primer – obtained from Professor Robert Nibbs (19)
- 11wt5 primer – obtained from Professor Robert Nibbs (19)

Buffers and Solutions

- **Endogenous blocking solution:** 10% serum + 1% BSA PBS

- **Triton X blocking solution:** 0.3% triton X + 1% BSA PBS
- **Biotin block solution:** 0.0033% biotin + PBS
- **Avidin block solution:** 0.033% avidin + PBS
- **Tween-20 blocking solution:** 0.5% tween-20 + 1% BSA PBS
- **FACS buffer:** DPBS, 2% FCS, 1mH EDTA, 0.06% sodium azide
- RPMI + 2% FCS
- **1.5% agarose gel:** 1.5g agarose + 100ml 5x TBE buffer + 20µl SYBR® safe DNA gel stain
- **PCR lysis buffer:** 25mM sodium hydroxide, 0.2mM EDTA
- **PCR neutralising buffer:** 40mM Tris-HCL (pH≈5), DNAse-free water

Additional Materials

- Streptavidin-Alexa Fluor® 555 conjugate – Invitrogen ♯S32355
- Penicillin-Streptomycin – Gibco ♯15070-063
- 10% Fetal Bovine Serum – Gibco ♯10437-028
- TripLE™ Express (+phenol red) – Gibco ♯12605-028
- Paraformaldehyde (PFA) – Sigma-Aldrich ♯158127
- Microscope cover slips – Menzel-Gläser ♯BB024032A1
- Dulbecco's Phosphate Buffered Saline (DPBS) – Sigma ♯D8662
- Dulbecco's Phosphate Buffered Saline (DPBS) (-calcium/magnesium) – Sigma ♯D8537
- Phosphate Buffered Saline (PBS) tablets – Sigma-Aldrich ♯P4417-100TAB
- Triton X-100 – VWR International
- Tween-20 – Fischer Scientific
- Prolong® gold anti-fade reagent – Invitrogen ♯P36930

- Agarose, for routing use – Sigma-Aldrich ♯A9539-500G
- Probumin® bovine serum albumin powder (BSA) – Millipore ♯82-045-1
- Biotin powder – Sigma-Aldrich ♯B4639
- Streptavidin – Sigma-Aldrich ♯S4762
- Methanol, laboratory reagent grade – Fischer Scientific ♯M/3950/17
- DAPI – Invitrogen ♯D1306
- Goat serum – Sigma-Aldrich ♯G9023-10ml
- Donkey Serum – Sigma-Aldrich ♯D9663-10ml
- Multispot microscope slides – Henley Essex ♯PH-005
- 70µm cell strainer – BD Falcon™ ♯352350
- Deoxyribonucleotide triphosphate (dNTP) mix – Bioline ♯BIO-39053
- NH_4 PCR reaction buffer – Bioline ♯BIO-37025
- $MgCl_2$ solution – Bioline ♯BIO-37026
- RNAse-free water – Qiagen ♯129112
- Biotaq® DNA polymerase – Bioline ♯BIO-21041
- 100bp DNA ladder – New England Biolabs ♯N3231S
- SYBR safe DNA gel stain – Invitrogen ♯533102
- Acetone – Sigma-Aldrich ♯179124
- Trypsin/Ethylenediaminetetraacetic acid (EDTA) – Invitrogen #15400-054
- Ultrapure 10x TBE buffer – Gibco ♯15581-044
- Collagenase D – Roche ♯11088858001
- DNAse – Roche ♯112649322001
- Near infrared cell death stain – Invitrogen ♯L10119
- Aqua fluorescent reactive dye – Invitrogen ♯L34960

- Firefly D-Luciferin, potassium salt – Caliper Life Sciences ♯119222
- Puromycin (10μg/ml) – Sigma ♯P9620
- Geneticin (50μg/ml) – Gibco ♯10131-019

Murine Lymph Node Tissue Sections

Tissue section	**Additional Information**
4/12 Inguinal Lymph Node	Wild-type Non-tumour bearing
3/12 Inguinal Lymph Node	CCRL1-knockout Non-tumour bearing
275/11 Inguinal Lymph Node	Wild-type $CCR7^+$ tumour bearing
276/11 Inguinal Lymph Node	Wild-type $CCR7^+$ tumour bearing
272/11 Inguinal Lymph Node	CCRL1-knockout $CCR7^+$ tumour bearing
274/11 Inguinal Lymph Node	CCRL1-knockout $CCR7^+$ tumour bearing
273/11 Inguinal Lymph Node	CCRL1-knockout $CCR7^+$ tumour bearing
278/11 Inguinal Lymph Node	Wild-type $CCR7^+$ tumour bearing
279/11 Inguinal Lymph Node	Wild-type $CCR7^+$ tumour bearing
280/11 Inguinal Lymph Node	CCRL1-knockout $CCR7^+$ tumour bearing
257/11 Inguinal Lymph Node	Wild-type $CCR7^+$ tumour bearing
258/11 Inguinal Lymph Node	Wild-type $CCR7^+$ tumour bearing
259/11 Inguinal Lymph Node	Wild-type $CCR7^+$ tumour bearing
25/12 Inguinal Lymph Node	CCRL1-knockout Non-tumour bearing
26/12 Inguinal Lymph Node	Wild-type Non-tumour bearing
9/12 Inguinal Lymph Node	CCRL1-knockout Non-tumour bearing
10/12 Inguinal Lymph Node	Wild-type Non-tumour bearing
141/11 Inguinal Lymph Node	CCRL1-knockout C57BL/6 non-CCR7 tumour bearing

2.2 Methods

2.2.1 Mouse Strains

C57BL/6 mice and CCRL1-/- mice were obtained from Dr. Robert Nibbs (19). Mice were housed at the Biomedical Services Unit (University of Birmingham, UK) in accordance with institutional and National Institutes of Health guidelines.

2.2.1.1 PCR Genotyping

The knockout-mice generated and used in these experiments were of a heterozygous breed. It was therefore necessary to characterize the mice to determine their genotype. The genotypes were identified by PCR of genomic DNA prepared from ear-punch tissue. The tissue was firstly lysed with 75µl of PCR lysis buffer at 95°C for 20 minutes. The lysis buffer was then inactivated upon addition of 75µl of PCR neutralising buffer and the samples vortexed briefly. A 2µl aliquot was taken and added to 10µl of PCR reaction master mix. The primer sets used are listed in Appendix A: Table 1. The samples were then centrifuged for 30 seconds at 1000rpm before being PCR amplified. The 1.5% agarose gels were prepared on the day of use and were loaded with 10µl of sample DNA and 10µl of 100bp DNA ladder. They were then run at +80V for approximately 30 minutes and then analysed using SYBR safe DNA gel stain.

2.2.2 Characterisation of B16-CCR7 Melanoma Cell Line

2.2.2.1 Cell Culture

The highly metastatic B16-F1 and CCR7-transfected B16-F1 (B16-CCR7) melanoma cell lines were routinely cultured in DMEM media supplemented with 10% FBS, penicillin-streptomycin and L-glutamine. Cell cultures were incubated at 37°C in

a humidified atmosphere containing 5% CO_2 in air until confluent. Cells were detached using 2ml of TripLE™ Express for 2-3 minutes at 37°C and harvested in 8ml of complete media. The cell suspension was then centrifuged for 4 minutes at 250g (1076rpm) and the supernatant aspirated. For cell culture maintenance, the cell pellet was resuspended in 10ml of complete media and a 1:12 dilution carried out. The appropriate volume of cell suspension was then transferred to a vented 75cm^3 tissue culture flask containing pre-warmed media. The B16-CCR7 cell line was selected for both CCR7 and luciferase expression by addition of geneticin (1000µg/ml) and puromycin (2µg/ml).

2.2.2.2 Flow Cytometry

For Flow Cytometry, cells were scraped off the 75cm^3 tissue culture flask into 1ml of cold PBS using a cell scraper. The cells were then centrifuged at 300g for 4 minutes and the supernatant discarded. The cell pellets were resuspended in 500µl RPMI 2% FCS containing collagenase D (1:50) and DNAse (1:200) and incubated at 37°C for 10 minutes with gentle shaking. After 10 minutes, 5µl of EDTA was added and the cell suspensions were left on ice for 5 minutes before being passed through a 70µm cell strainer, followed by 5ml of FACS buffer. The cells were then counted and seeded at $0.5x10^6$ cells/well in to a clear, round-bottom 96-well plate. Prior to staining, the cells were incubated on ice for 10 minutes with anti-CD16/32 antibody to block the Fc receptors. A PE-conjugated anti-CCR7 antibody and a near infrared cell death stain were used to stain the cell suspensions and to gate out non-viable cells. Immunostained cells were then analysed using the Beckman Coulter CyAn™ ADP analyser and FlowJo software.

2.2.3 Evaluation of B16-CCR7 Melanoma Cell Line

2.2.3.1 Seeding Cells For Intravital Imaging

B16-F1, parental B16-CCR7 (non-selected) and puromycin-/geneticin-selected B16-CCR7 cells were seeded into a black-walled 96-well tissue culture plate at a 1:2 titration with a starting concentration of $1x10^5$ cells/ml. The cells were incubated overnight at 37°C to allow them to adhere. Prior to imaging, the media was aspirated and replaced with 100µl/well of D-luciferin diluted in complete media. The plates were imaged using the IVIS® Spectrum intravital microscope (Caliper Life Sciences) and analysed using the IVIS® Living Image software (Caliper Life Sciences). Region-of-interest (ROI) measurements were exported to Microsoft Excel. Graphs were generated in Microsoft Excel by plotting the ROI values for each experimental condition.

2.2.3.2 Inoculation of Mice With B16-CCR7 Melanoma Cells

B16-F1 and puromycin-/geneticin-selected B16-CCR7 cells were harvested by trypsinisation and washed in cold PBS. The cells were then counted and resuspended at $60x10^6$ cells/ml in the appropriate volume of cold PBS. The cells were filtered through a 70µm cell strainer and the volume readjusted, if necessary, to reach a final concentration of $50x10^6$ cells/ml. For ear injections, 20µl of cell suspension was injected into the subcutaneous space under the central dorsal surface of the ears of both wildtype (WT) and CCRL1-/- C57BL/6 mice. Mice were sacrificed after 3 weeks of growth.

2.2.3.3 Intravital Microscopy

Prior to anaesthetisation, mice were weighed and received D-Luciferin via i.p. injection (10µl per kg body weight). After 5 minutes, the mice were anaesthetised with 2.5% isoflurane and prepared for intravital imaging by shaving the area surrounding the ears. The mice were imaged using the IVIS® Spectrum intravital microscope (Caliper Life Sciences) and the images analysed using IVIS® Living Image software (Caliper Life Sciences). The tumour diameter and radius was also measured using a caliper. ROI measurements were exported to Microsoft Excel and graphs generated by plotting the ROI values for each mouse versus the tumour diameter or tumour radius.

2.2.4 Immunofluorescence

2.2.4.1 Immunofluorescent Detection of Tumour Cells

Serial lymph node sections with a thickness of 6µm were cut using a cryostat, mounted on to slides and air-dried for 30 minutes before being stored at -80°C. Before use, sections were fixed in methanol on ice for 10 minutes, air-dried for 30 minutes and then hydrated in PBS. Prior to staining, sections were treated separately with avidin (1:30) and biotin (1:6) for 15 minutes at room temperature to prevent any non-specific staining. In order to block endogenous Fc receptors, sections were also incubated for 15 minutes at room temperature with an endogenous blocking solution containing 10% normal serum derived from the host species of the secondary antibody. All antibodies were diluted in this endogenous blocking solution.

Rabbit anti-mouse TRP-2 antibody (1:1000) was applied to the sections for 40 minutes at room temperature. Sections were then washed for 10 minutes with PBS and incubated with goat anti-rabbit biotinylated antibody (1:500). After a 30 minute incubation at room temperature the sections were washed in PBS and Streptavidin-Alexa Fluor® 555 conjugate (1:500), rat anti-mouse CD45R (B220) eFluor® 450

(1:25), rat anti-mouse Lyve-1 eFluor® 660 (1:50) and mouse anti-mouse CD45.2-FITC conjugated antibody (1:50) applied to the sections for 30 minutes at room temperature shielded from light. Negative control sections were treated under equivalent conditions with no primary antibodies and were counterstained with DAPI. Slides were mounted with Prolong Gold mounting media and were visualised using a Zeiss LSM 510 Meta confocal microscope. Images were analysed using the Zeiss LSM Image Browser software and then exported to Microsoft Powerpoint.

Several different methods for staining tumour cells in the lymph node were tested, however, all results described were generated using the staining protocol outlined above. Previously tested methods included fixing lymph node sections in acetone at 4°C for 20 minutes followed by direct staining of tumour cells with streptavidin-Alexa Fluor® 488, however this method resulted in non-specific staining of adipose tissue surrounding the lymph node. Lymph node sections were also stained using an anti-mouse Melanoma (HMB45 + DT101 + BC199) antibody followed by the Vector® Mouse On Mouse (MOM) Immunodetection kit (Vector Laboratories), however there was significant non-specific staining of the B cell areas.

2.2.4.2 Immunofluorescent Detection of CCL21

Serial lymph node sections were fixed in 4% paraformaldehyde for 10 minutes at room temperature, washed in PBS for 10 minutes and endogenous Fc receptors blocked with endogenous blocking solution. For the detection of extracellular CCL21, goat anti-mouse CCL21 (1:15), rat anti-mouse PNad (1:50) and rabbit anti-mouse Lyve-1 (1:100) were diluted in endogenous blocking solution and applied directly to the sections for 45 minutes at room temperature. After a 10 minute PBS wash step, the sections were incubated with Alexa Fluor® 488 donkey anti-rat antibody (1:300), Alexa Fluor® 647 donkey anti-goat antibody (1:100) and Alexa Fluor® 555 donkey anti-rabbit

antibody (1:500) diluted in endogenous blocking solution for 30 minutes at room temperature shielded from light. Following this, the sections were washed in PBS for 10 minutes, counterstained with DAPI and mounted.

For intracellular detection of CCL21, sections were permeabilised using 0.3% triton X-100 for 15 minutes at room temperature prior to incubation with the primary antibodies. All antibodies used were diluted in 0.3% triton X-100.

2.2.4.3 Immunofluorescent Detection of CCRL1

Sections were fixed in acetone at 4°C for 20 minutes, air-dried for 30 minutes and blocked with endogenous blocking solution. Goat anti-mouse CCRL1 (1:50) and hamster anti-mouse CD11c-FITC conjugated antibody (1:50) were prepared in tween-20 and then applied to the sections for 45 minutes at room temperature. After a 10 minute PBS wash step, the sections were incubated with Alexa Fluor® 555 donkey anti-rabbit antibody (1:500), rabbit anti-FITC 488 conjugated antibody (1:200) and rat anti-mouse Lyve-1 eFluor® 660 (1:50) for 30 minutes at room temperature shielded from light. Sections were then washed in PBS for 10 minutes, counterstained with DAPI and mounted.

2.2.5 Data Analysis

Images were exported to and analysed using the LSM 510 software package. Raw data was exported to excel and graphs generated by plotting ROI values for each experimental condition against cell number or tumour size.

3. AIMS AND OBJECTIVES

The main objective was to investigate CCR7-driven metastasis and survival in the lymph node and whether host CCRL1 expression in the lymph node affects these processes. Further research included the inoculation of B16-F1 cells transduced with CCR7 and luciferase in the ear skin of WT and CCRL1-KO mice to evaluate the kinetics of tumour growth at the inoculation site and within tumour-draining lymph nodes.

4. RESULTS

4.1. Immunofluorescent Detection of Tumour Cells in the Lymph Node

4.1.1. Development of an Experimental Protocol That Allows the Early Detection of B16 Melanoma in the Lymph Node

The identification of metastatic melanoma in the sentinel LN has traditionally involved haematoxylin and eosin (H&E) staining of LN sections. Although it is possible to detect, with ease, larger metastatic foci in H&E-stained sections, smaller metastatic clusters and sparse isolated cells associated with early metastasis may be missed. HMB-45, a monoclonal antibody directed against melanoma antigen, represents another widely used immunohistochemical staining technique that is regarded by some to be a useful tool in the detection of human primary and early metastatic melanoma (30). The antibody has been known to react with melanoma cells, junctional nevus cells and foetal melanocytes but not with other non-melanoma malignancies, thus demonstrating sound specificity (30). Although the antibody is known to cross-react with mouse melanoma, the sensitivity of the antibody for melanoma cells has come into question and it may not provide a reliable means for the detection of single isolated tumour cells (30). It was therefore, necessary to develop a more precise and reliable method of staining melanoma cells in early murine LN metastasis.

Previous work within the group had suggested that B16 melanoma cells bind to streptavidin with high affinity. In order to investigate whether streptavidin staining would be suitable for the detection of B16 melanoma cells in the LN, murine WT and CCRL1-KO inguinal LN sections, both tumour bearing and non-tumour bearing, were

stained with a streptavidin-fluorophore conjugate. Streptavidin-positive cells were found to be closely associated with the subcapsular sinus but were also found to be present in non-tumour bearing sections, thus demonstrating non-specific binding (Figure 4.1).

Staining was next attempted using a murine monoclonal antibody raised against melanoma antigens (HMB-45, DT101, BC199). In an attempt to minimise any background staining, the Vector® MOM immunodetection kit was employed and used according to the manufacturer's guidelines, however, non-specific staining was noted in non-tumour draining mesenteric LNs (Figure 4.2). Staining persisted in sections that were not treated with the primary antibody.

Mesenteric LN sections were also stained using a rabbit polyclonal anti-TRP-2 primary antibody after blocking endogenous biotins. TRP-2 is an enzyme involved in melanin biosynthesis and is highly expressed by melanocytes (31,32). TRP-2-positive staining was identified in all melanoma tumour sections, with relatively low background staining in mesenteric LNs (Figure 4.3).

4.1.2. Optimisation of B16 Melanoma Staining in the Lymph Node

WT inguinal LN sections were stained for both TRP-2 and the hematopoietic specific marker CD45 to better differentiate the B16 melanoma cells from the hematopoietic cells within the lymph node. Sections were also counterstained with the nuclear dye, DAPI, to confirm the presence of tumour cells based upon differences in cell nuclear morphology. Large tumour foci were clearly visible upon inspection of both DAPI (data not shown) and TRP-2 staining (Figure 4.4). Furthermore, these foci were largely devoid of CD45 staining with the exception of a few scattered, $CD45^{high}$ $TRP\text{-}2^{-}$ cells. Many of the LNs also displayed isolated, scattered $TRP\text{-}2^{+}$ cells in close

proximity with the subcapsular sinus, of which some were identified as being positive for CD45 also.

4.1.3. The effect of host CCRL1 expression on metastatic establishment and distribution of CCR7-expressing B16-F1 (B16-CCR7) melanoma in the lymph node

Having established the optimal staining conditions, it was possible to investigate where B16-CCR7 melanoma establishes in the lymph node and whether CCRL1 expression could influence melanoma establishment and distribution. WT and CCRL1-KO tumour bearing LNs were stained according to the protocol described in section 2.2.4.1. Histological analysis of LN sections indicated that CCR7-expressing B16 melanoma preferentially establishes within the B cell areas and also surrounding the efferent lymphatic vessels of the LN (Figure 4.5a and b). CCRL1 expression did not appear to alter the growth or distribution of B16-CCR7 melanoma within the LN. Eight of eight WT LNs and four of six CCRL1-KO LNs showed tumour foci in the B cell area (Figure 4.5c). Anti-TRP-2 staining was negative in the fifth CCRL1-KO LN (data not shown) and the sixth CCRL1-KO LN displayed scattered B16-CCR7 melanoma cells throughout the cortex and medulla (Figure 4.5a and b). Once again, brightly stained $CD45^{high}$ $TRP\text{-}2^{-}$ cells were found to be dispersed within the foci (Figured 4.5b).

4.1.4. Characterisation of the Metastatic B16-CCR7 Melanoma Tumour Microenvironment

In an attempt to further characterise the $CD45^{high}$ $TRP\text{-}2^{-}$ cells present within the tumour foci, serial inguinal LN sections were stained with a panel of common immune

cell markers. Relatively few $CD3^+$ cells were present within metastatic foci (Figure 4.6). Conversely, large proportions of $CD4^+$ cells were present, both within and surrounding the foci. However, the relatively few $CD3^+$ cells within the foci suggests that these cells may not necessarily represent T cells. There were also no $FOXP3^+$ regulatory T cells present within the infiltrating T cells of the foci. A large number of $CD8^+$ cells were, however, detected in the LN sections, mostly surrounding the foci. Relatively little CD11c or CD11b staining was detected. No noticeable differences in staining were observed in WT and CCRL1-KO LNs for any of the immune cell markers tested (Figure 4.6 a and b).

4.2. The Effect of Host CCRL1 Expression on CCL21 Protein Levels and Distribution in the Lymph Nodes of Tumour Bearing and Non-Tumour Bearing Mice

4.2.1. CCL21 Expression in PFA-Fixed Lymph Node Sections Permeabilised with Triton-X

Next we sought to address whether CCL21 expression is altered in tumour bearing LNs in the presence or absence of CCRL1 expression. Inguinal LN sections were permeabilised with triton-X and stained for CCL21 according to the protocol outlined in section 3.2.4.2. CCL21 expression appeared to be downregulated in the subcapsular sinus of both tumour bearing WT and CCRL1-KO LNs when compared with non-tumour bearing WT LNs (Figure 4.7). Of note, Langerin cells accumulated within the subcapsular sinus of CCRL1-KO LNs, which is in concordance with unpublished data from the group.

4.2.2. CCL21 Expression in PFA-Fixed Non-Permeabilised Lymph Node Sections

CCL21 expression was also assessed in non-permeabilised LN sections. Again, expression appeared to be downregulated in the sinus of tumour bearing WT and CCRL1-KO LN sections when compared to non-tumour bearing WT and CCRL1-KO LN sections, thus suggesting that LNs bearing micrometastases may inhibit CCL21 expression (Figure 4.8a). Interestingly, presence of CCL21 in the tumour was also observed (Figure 4.8b).

4.3. CCRL1 Expression in the Lymph Nodes of Tumour Bearing and Non-Tumour Bearing Mice

LN sections were then stained for CCRL1 according to the protocol described in section 2.2.4.3 to ascertain whether expression is altered in tumour bearing LNs. Similarly, CCRL1 expression appeared to be reduced in the sinus of WT tumour bearing LNs when compared with WT non-tumour bearing LNs (Figure 4.9), suggesting that LNs bearing micrometastases may also suppress the expression of CCRL1.

4.4. Establishment of CCR7-Expressing B16-F1 (B16-CCR7) Melanoma in Wild-Type and CCRL1-Knockout Mice

As the majority of the LNs displayed large, well-defined metastases it was not possible to examine the kinetics of B16 melanoma tumour growth and to assess the

effect of CCRL1 on the CCR7-CCL19/21 chemokine axis in early LN metastasis *in vivo*. In order to address this, B16 melanoma cells transduced with CCR7 and luciferase (B16-CCR7) were utilised. Previous work in the group has demonstrated that the cells express CCR7 to a significantly higher level than control B16-F1 cells (unpublished data). The levels of other chemokines and their receptors were also measured and it was revealed that the cells were negative for the expression of CXCR4, CXCR5, CCR9, CCL19, CCL21, CXCL13 and CXCL12 (unpublished data).

In this small tumour experiment, the cells were exposed to antibiotic selection to enhance tumour cell expression of luciferase and to eliminate $CCR7^-$ melanoma cells. These cells were then injected in to the ears of both WT and CCRL1-KO C57BL/6 mice and early tumour cell behaviour monitored by luciferase activity using the IVIS Spectrum® intravital microscope.

4.4.1. PCR Genotyping

Initial experiments involved determining the genotype of the mice so that WT and CCRL1-homozygous KO mice could be identified and selected for inoculation. The genotype was determined by PCR using two forward primers, each one distinct for the KO or WT allele, and a common reverse primer. The WT allele was present at 610bp and the KO allele at 420bp. Of the 23 mice genotyped, 5 were revealed to be WT, 7 were homozygous KOs and 11 were of a heterozygous nature (Figure 4.10). Mice taken forward for inoculation are marked with an asterisk (Figure 4.10b).

4.4.2. Optimisation of the Expression of Luciferase and CCR7 in the B16-CCR7 cell line

Luciferase activity in B16-CCR7 cells was assessed using the IVIS Spectrum® intravital microscope and converted into luciferase expression based on cell counts. B16-F1 cells transduced with luciferase were shown to have the highest level of luciferase activity (Figure 4.11a – before selection). The B16-CCR7 cells showed much weaker activity and, as a result, may not have provided enough sensitivity to accurately follow and measure tumour development from a small number of B16 melanoma cells. In an effort to increase the sensitivity of the B16-CCR7 cell line, the cells were exposed to the antibiotic, puromycin to select for high luciferase-expressing cells. Parental B16-CCR7 cells were not selected with puromycin. Unfortunately, selection did not result in enhanced luciferase activity (Figure 4.11a – after selection).

B16-CCR7 cells were also exposed to the antibiotic, geneticin, in order to select for CCR7 expression. Once again, parental B16-CCR7 cells were not selected with geneticin. Although, antibiotic selection did not eliminate the population of $CCR7^{low}$ cells, it did result in a shift in CCR7 expression in $CCR7^{+}$ cells towards much higher levels (Figure 4.11b).

4.4.3. Ear Injection of B16-CCR7 Cells in Wild-Type and CCRL1-Knockout Mice

Following optimisation, B16-CCR7 cells were injected in to the ears of 4 WT and 3 CCRL1-KO C57BL/6 mice to compare metastasis kinetics between the groups. After 7 days, the mice were examined for the accumulation of B16-CCR7 cells in the ear. All CCRL1-KO mice displayed established tumours at the site of injection (not shown). Interestingly, none of the WT mice had visible tumours at this stage, suggesting that CCRL1 may play a protective role in the early stages of primary

tumour formation. After an additional 11 days, the mice were examined again. Only 1 of the 4 WT mice had a visible tumour at the site of injection (not shown).

To evaluate the sensitivity of the B16-CCR7 cell line, the CCRL1-KO mice were imaged using the IVIS Spectrum® intravital microscope, 18 days post-inoculation. Primary tumours were detected but no LN metastases were visible (Figure 4.12a). The overall size of each primary tumour was also measured and was shown to bear no correlation with luciferase expression, with the smallest tumour (mouse #0) appearing to have the greatest level of luciferase activity (Figure 4.11b). For this reason, the cell line would not be suitable for the non-invasive detection and quantification of tumour cells *in vivo*.

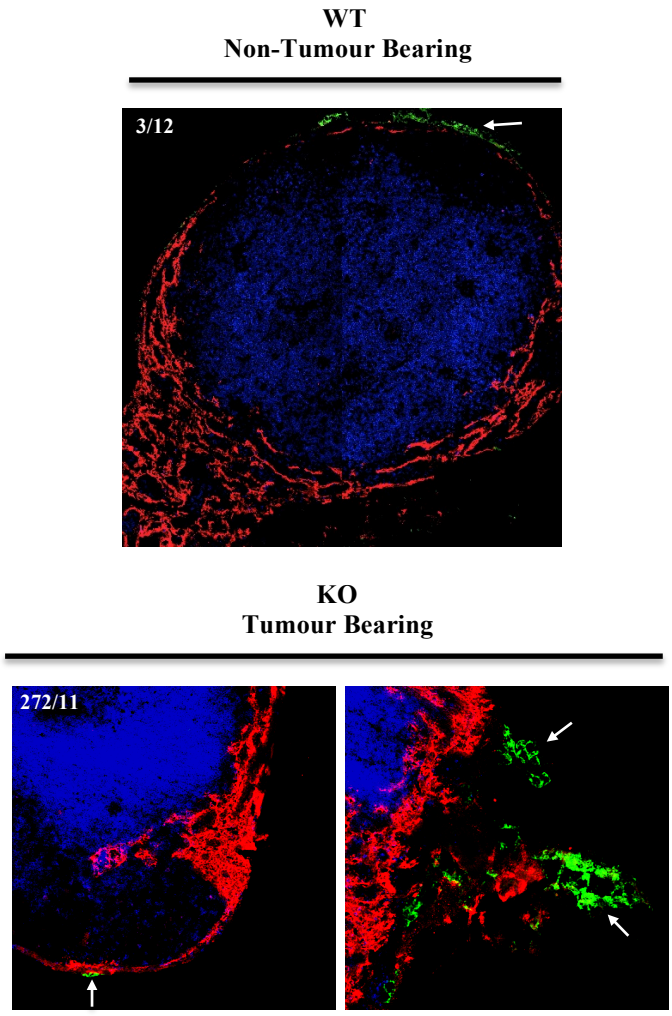

Figure 4.1: Direct Immunofluorescent Staining of Lymph Node Sections Using a Streptavidin-Fluorophore Conjugate.

Representative images of inguinal lymph node sections from WT and CCRL1-KO C57BL/6 mice. CCRL1-KO mice received $1x10^5$ CCR7-expressing B16-F1 melanoma cells via subcutaneous injection. Mice were sacrificed after 3 weeks and serial lymph node sections cut and frozen. Frozen sections were acetone-fixed for 20 minutes at 4°C and then stained for the presence of $CD4^+$ T cells (blue), $LYVE\text{-}1^+$ lymphatic vessels (red) and streptavidin binding B16-F1 melanoma cells (green). Sections were then counterstained with DAPI and mounted using ProLong Gold. Images were taken at 10x (WT) and 25x (KO) magnification using the Zeiss LSM 510 confocal microscope. N=3 per group.

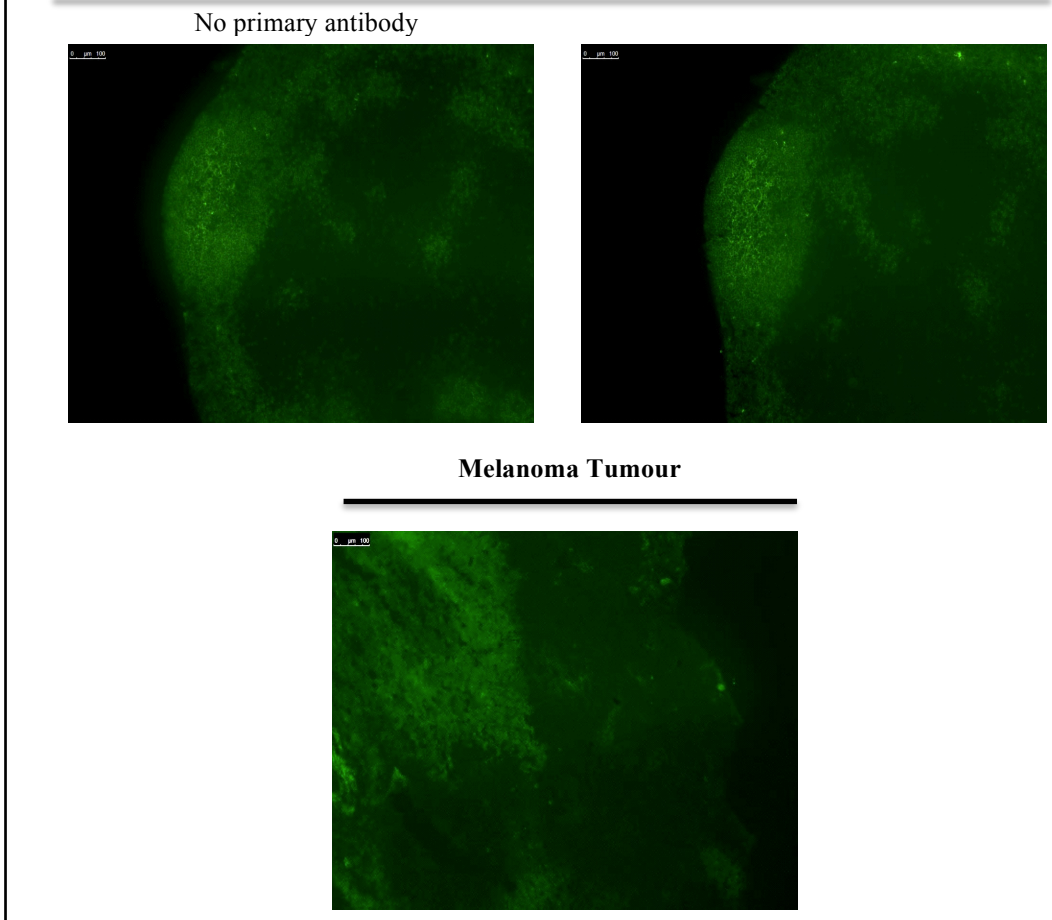

Figure 4.2: Indirect Immunofluorescent Staining of Lymph Node and Melanoma Tumour Sections Using an Anti-Melanoma Primary Antibody.

Representative images of mesenteric lymph node or melanoma tumour sections taken from WT C57BL/6 mice. Frozen sections were acetone-fixed for 20 minutes at 4°C and then stained using a melanoma antigen-specific (HMB45, DT101, BC199) primary antibody (green) at a concentration of $5x10^6$ mg/ml followed by the Vector® Mouse On Mouse (MOM) Immunodetection kit (Vector Laboratories). Sections were mounted using ProLong Gold and analysed at 10x magnification using the Leica DM6000 research microscope. N=1 per group.

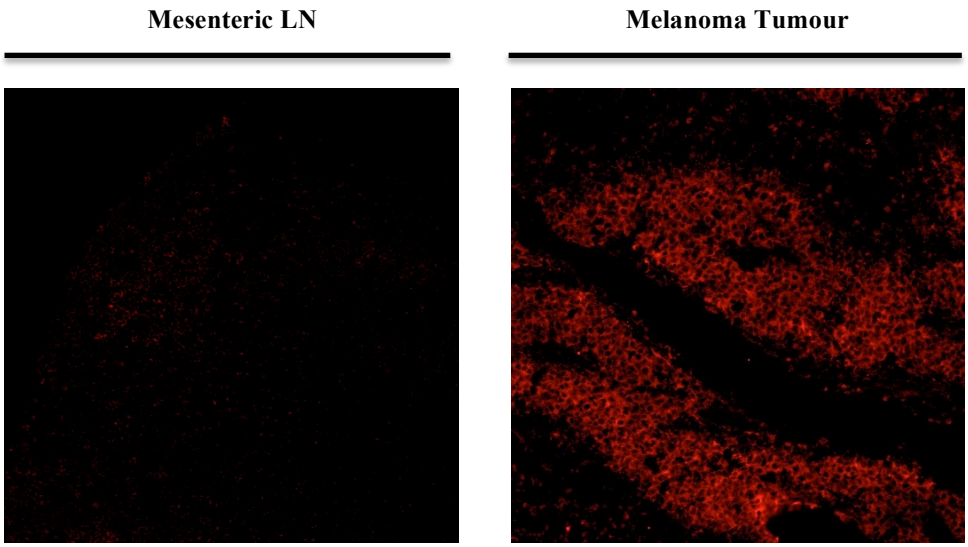

Figure 4.3: Indirect Immunofluorescent Staining of Lymph Node and Melanoma Tumour Sections Using an Anti-TRP2 Primary Antibody.

Mesenteric lymph node and melanoma tumour sections taken from WT C57BL/6 mice were methanol-fixed for 10 minutes at 4°C and stained with an anti-tyrosine related protein-2 (TRP-2) primary antibody at a concentration of 1µg/ml. Sections were then mounted using ProLong Gold and analysed at 25x magnification using the Zeiss LSM 510 confocal microscope. N=2 per group.

WT
Tumour Bearing

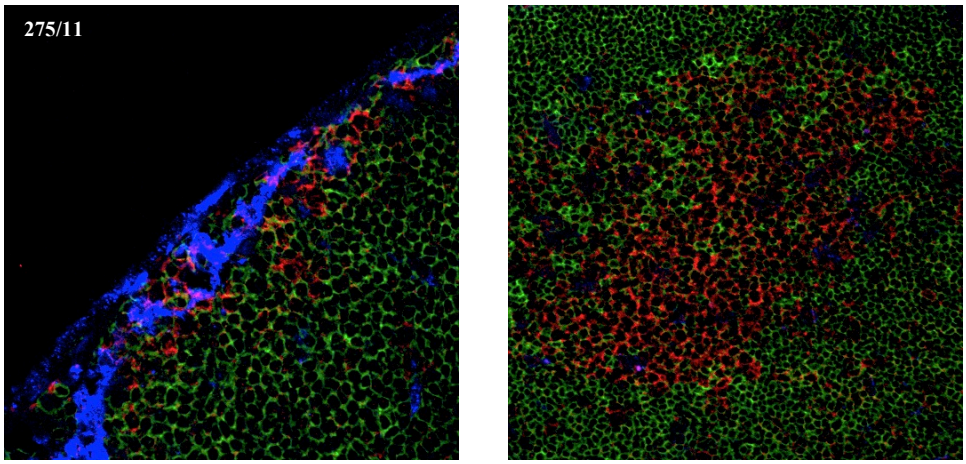

TRP-2 Lyve-1 CD45

Figure 4.4: Immunofluorescent Staining for TRP-2 and CD45 Enables the Accurate Identification of CCR7-expressing B16-F1 (B16-CCR7) Melanoma Cells in the Lymph Node.

Representative images of inguinal lymph node sections taken from WT C57BL/6 mice. Mice received $1x10^5$ CCR7-expressing B16-F1melanoma cells via subcutaneous injection. Mice were sacrificed after 3 weeks and serial lymph node sections cut and frozen. Frozen sections were methanol-fixed for 10 minutes at 4°C and stained for the presence of B16-CCR7 melanoma cells (red) using the anti-TRP-2 primary antibody at a concentration of 1µg/ml, LYVE-1^+ lymphatic vessels (blue) and $CD45^+$ immune cells (green). Sections were then counterstained with DAPI and mounted using ProLong Gold. Images were taken at 25x magnification using the Zeiss LSM 510 confocal microscope. N=1 per group.

a)

WT
Tumour Bearing

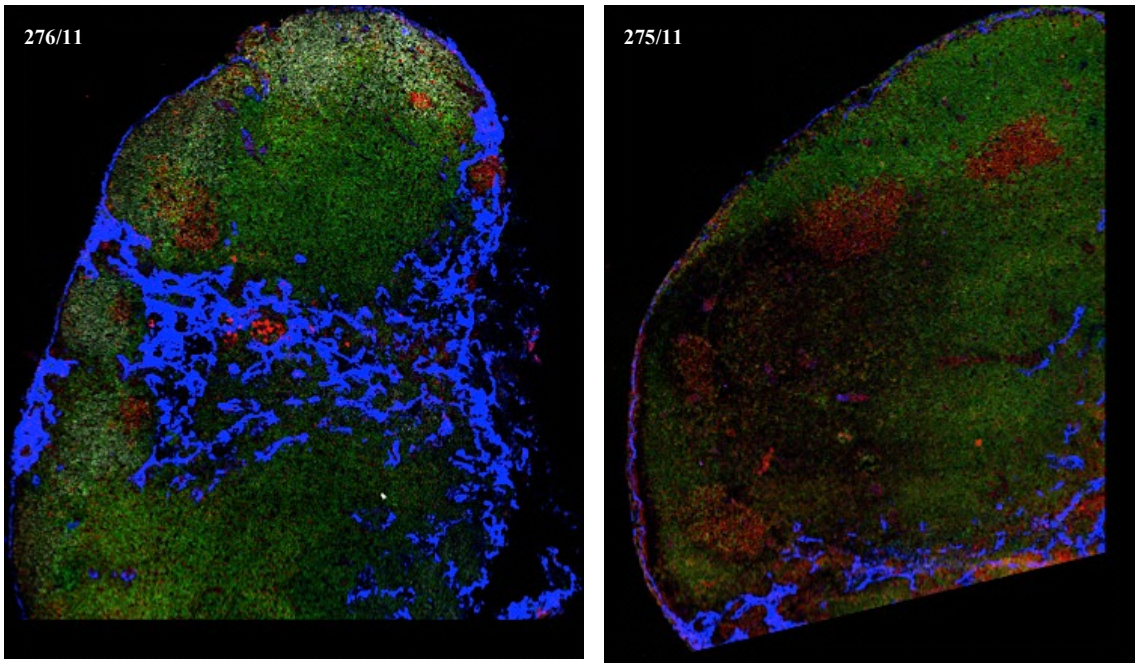

KO
Tumour Bearing

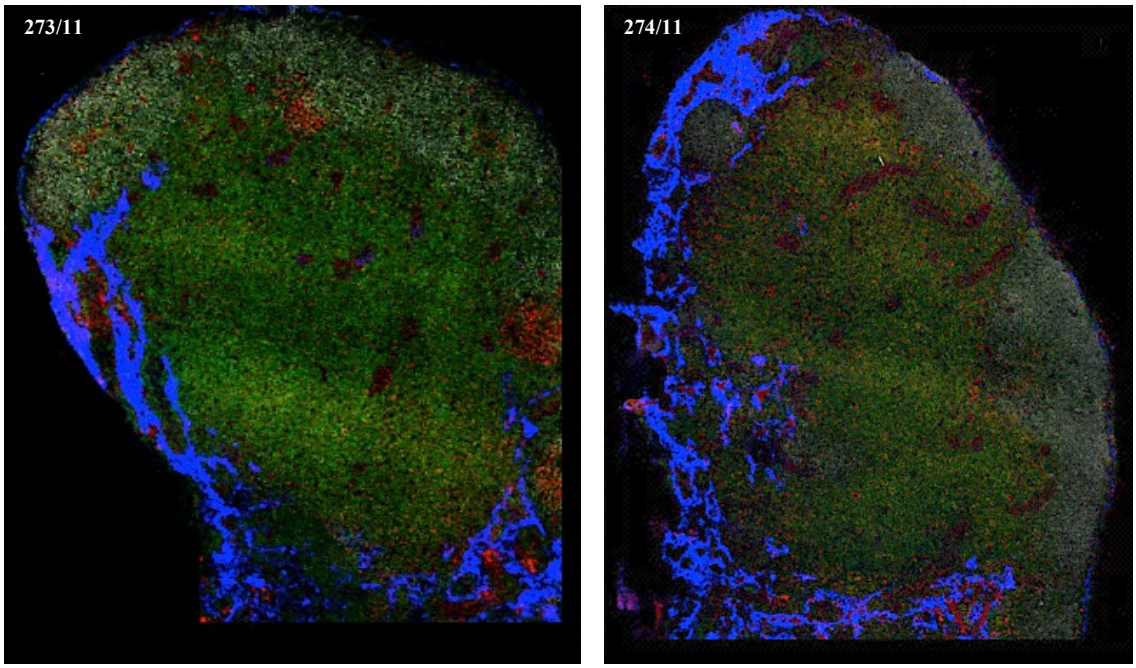

TRP-2 Lyve-1 CD45 B220

Figure 4.5a: Metastatic B16-CCR7 Melanoma Establishes Within the B Cell Areas of the Lymph Node.

a) Representative images of inguinal lymph node sections taken from WT and CCRL1-KO C57BL/6 mice. Mice received $1x10^5$ CCR7-expressing B16-F1 melanoma cells via subcutaneous injection. Mice were sacrificed after 3 weeks and serial lymph node sections cut and frozen. Frozen sections were methanol-fixed for 10 minutes at 4°C and stained for the presence of B16-CCR7 melanoma cells (red) using the anti-TRP-2 primary antibody at a concentration of $1x10^{-3}$ mg/ml, LYVE-1^+ lymphatic vessels (blue), $CD45^+$ immune cells (green) and $B220^+$ B cells (grey) (sections 259/11, 275/11 and 274/11 only). Sections were then mounted using ProLong Gold. Images were taken at 10x magnification using the Zeiss LSM 510 confocal microscope and merged together using Abode® Photoshop to create larger lymph node scans. N=3 per group.

b)

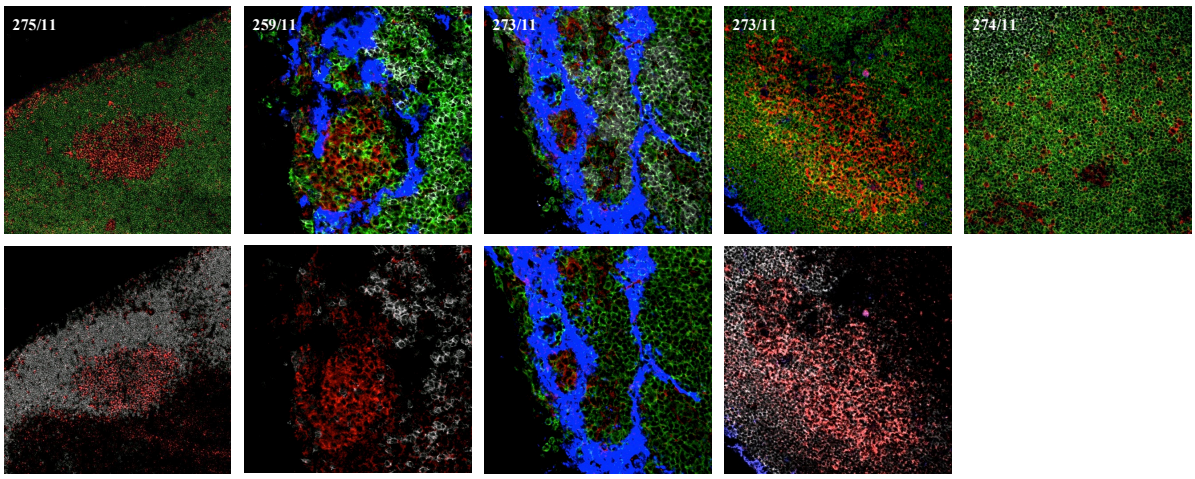

c)

Lymph Node Sections (# of LNs with metastatic foci/total # of LNs)	
Wild-Type (8/8)	**CCX-CKR1-Knockout (4/6)**
257	269
258	270
259	273
268	280
275	
276	
278	
279	

Figure 4.5b/c: Metastatic B16-CCR7 Melanoma Establishes Within the B Cell Areas of the Lymph Node.

b) Representative images of inguinal lymph node sections taken from WT and CCRL1-KO C57BL/6 mice. Mice received $1x10^5$ CCR7-expressing B16-F1 melanoma cells via subcutaneous injection. Mice were sacrificed after 3 weeks and serial lymph node sections cut and frozen. Frozen sections were methanol-fixed for 10 minutes at 4°C and stained for the presence of B16-CCR7 melanoma cells (red) using the anti-TRP-2 primary antibody at a concentration of $1x10^{-3}$ mg/ml, LYVE-1^+ lymphatic vessels (blue), $CD45^+$ immune cells (green) and $B220^+$ B cells (grey). Sections were then mounted using ProLong Gold. Images were taken at 10x, 25x and 40x magnification using the Zeiss LSM 510 confocal microscope. N= 8 per group for WT LNs. N=6 per group for CCRL1-KO LNs. **c)** Table showing the number of tumour bearing WT and CCRL1-KO lymph node sections displaying metastatic foci within the B cell zone.

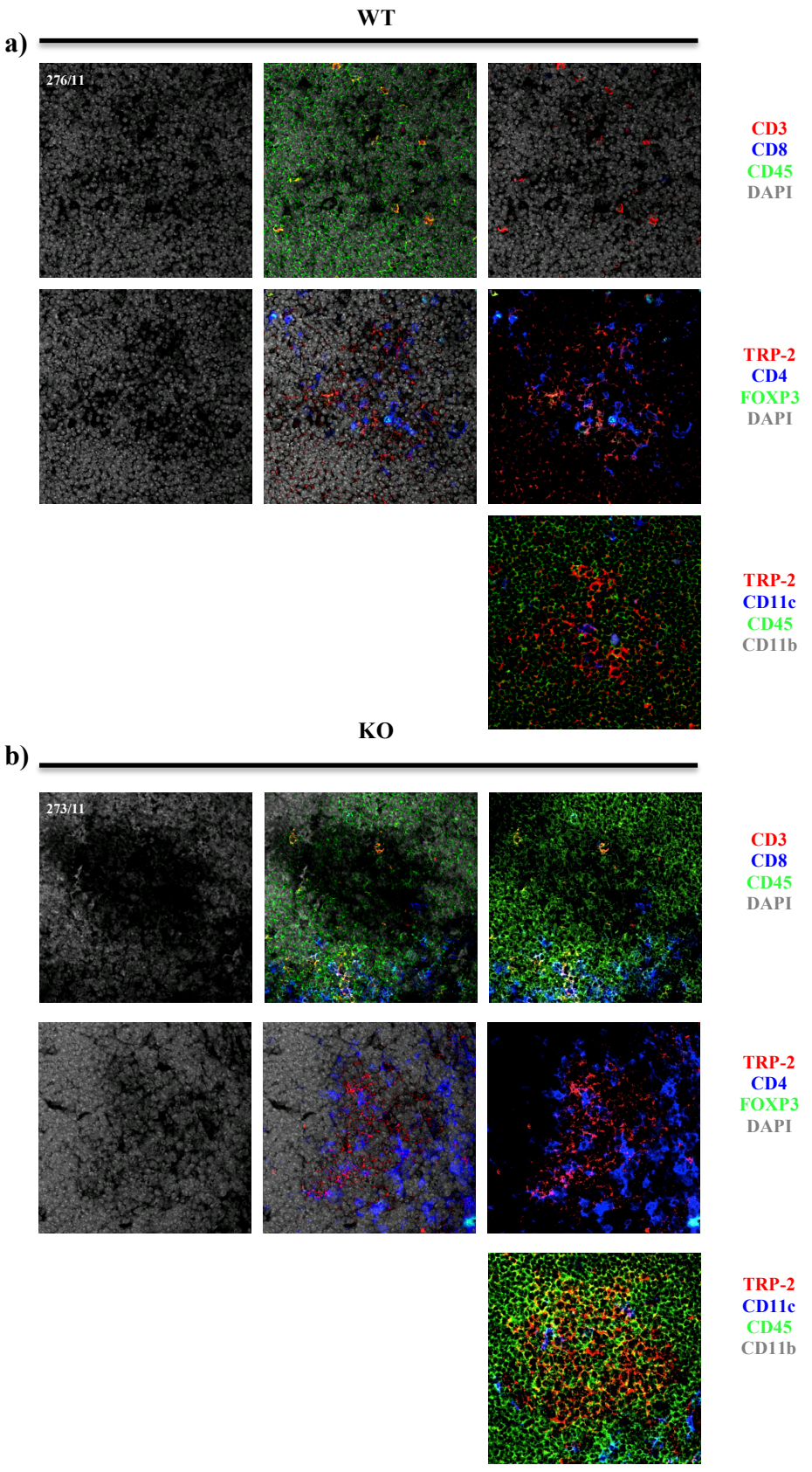

Figure 4.6: Immunofluorescent Staining of Tumour Bearing Lymph Node Sections for Common Immune Cell Markers.

a) Representative images of inguinal lymph node sections taken from WT C57BL/6 mice. **b)** Representative images of inguinal lymph node sections taken from CCRL1-KO C57BL/6 mice. Mice received $1x10^5$ CCR7-expressing B16-F1 melanoma cells via subcutaneous injection. Mice were sacrificed after 3 weeks and serial lymph node sections cut and frozen. Frozen sections were methanol-fixed for 10 minutes at 4°C and stained for various immune cell markers. Sections were then mounted using ProLong Gold. Images were taken at 40x magnification using the Zeiss LSM 510 confocal microscope. N=1 per group.

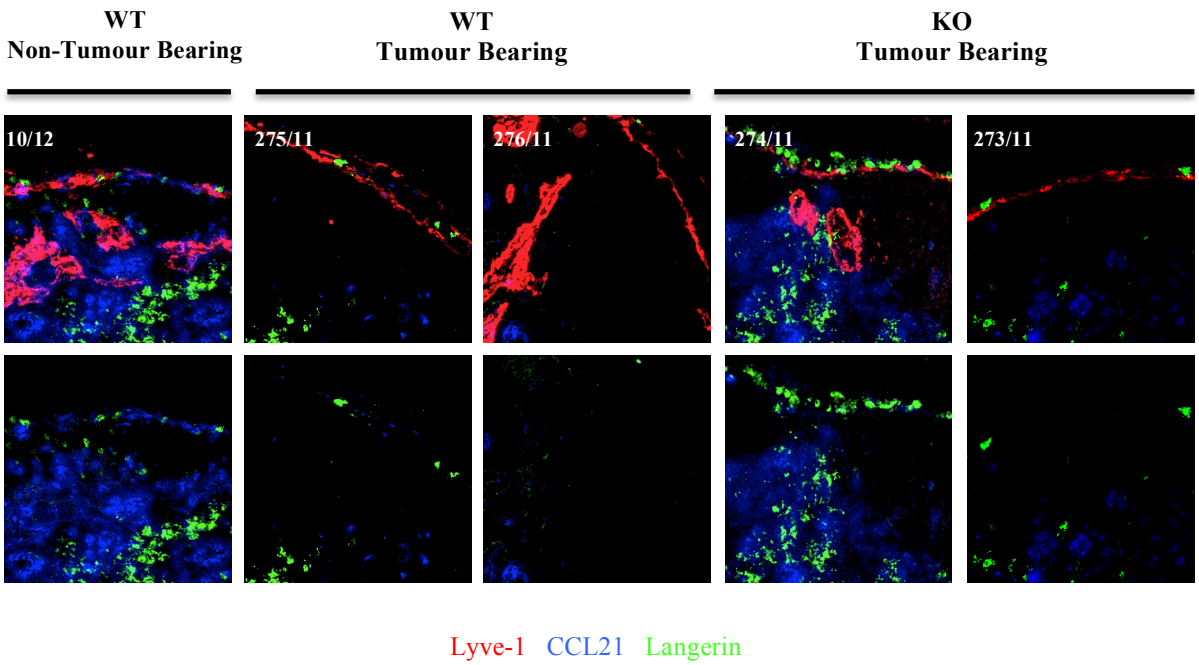

Figure 4.7: CCL21 Expression Appears to be Reduced in the Sinus of Permeabilised CCRL1-Knockout Lymph Node Sections.

Representative images of inguinal lymph node sections taken from WT and CCRL1-KO C57BL/6 mice. Mice received $1x10^5$ CCR7-expressing B16-F1 melanoma cells via subcutaneous injection. Mice were sacrificed after 3 weeks and serial lymph node sections cut and frozen. Frozen sections were fixed in 4% PFA for 10 minutes and permeabilised in 0.3% Triton-X100 before being stained for the presence of LYVE-1^+ lymphatic vessels (red), Langerin cells (green) and CCL21 (blue). Sections were then counterstained with DAPI and mounted using ProLong Gold. All images were taken at 25x magnification using the Zeiss LSM 510 confocal microscope. N=2 per group for tumour bearing LNs. N=1 for non-tumour bearing LNs.

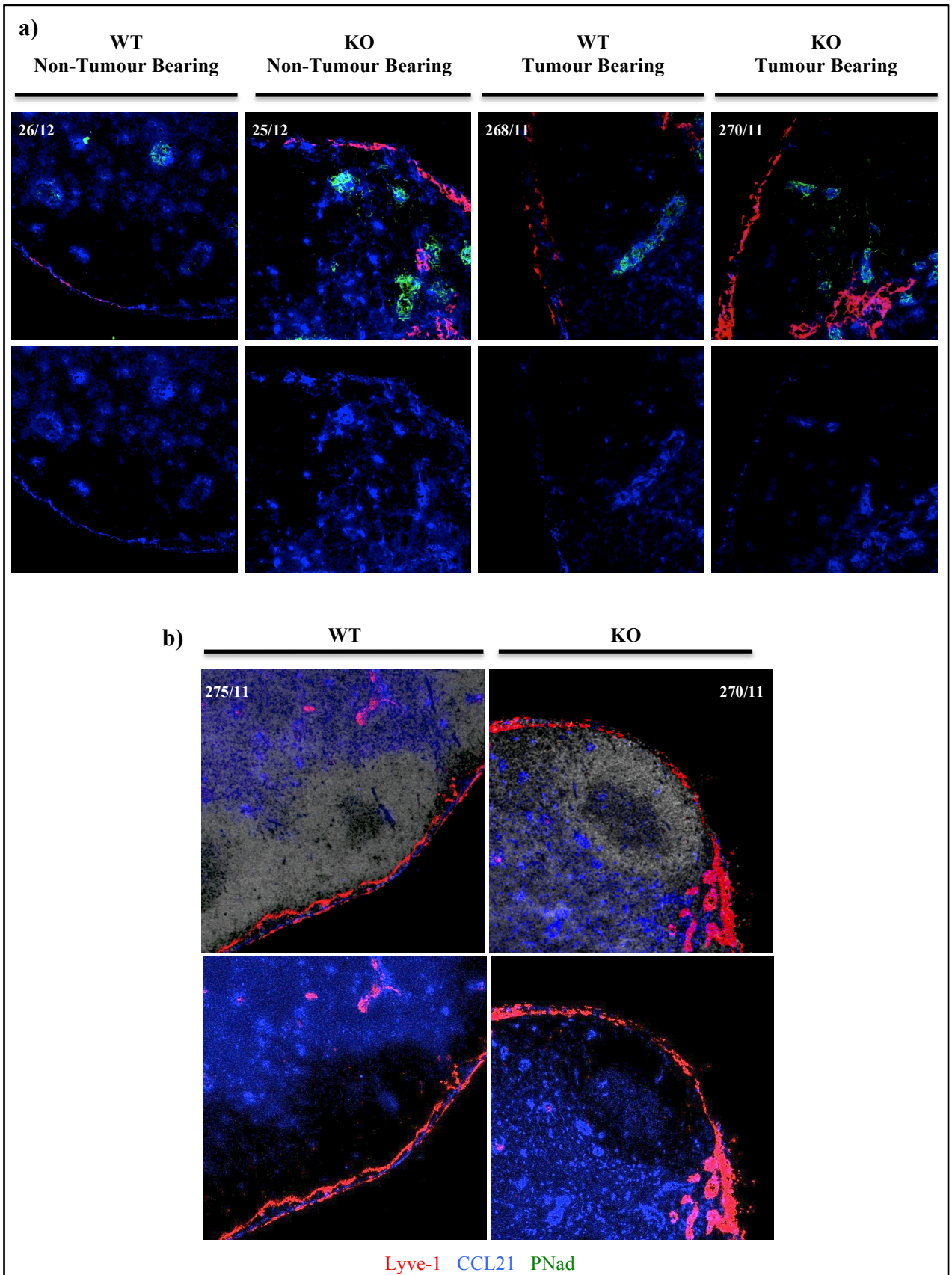

Figure 4.8: CCL21 Expression Appears to be Reduced in the Sinus of Non-Permeabilised CCRL1-Knockout Lymph Node Sections.

a) Representative images of inguinal lymph node sections taken from WT and CCRL1-KO C57BL/6 mice at 25x magnification. **b)** Representative images of inguinal lymph node sections taken from WT and CCRL1-KO C57BL/6 mice at 10x magnification. Mice received $1x10^5$ CCR7-expressing B16-F1 melanoma cells via subcutaneous injection. Mice were sacrificed after 3 weeks and serial lymph node sections cut and frozen. Frozen sections were fixed in 4% PFA for 10 minutes and stained for the presence of LYVE-1^+ lymphatic vessels (red), Langerin cells (green) and CCL21 (blue). Sections were then counterstained with DAPI and mounted using ProLong Gold. Images were taken using the Zeiss LSM 510 confocal microscope. N=3 per group for tumour bearing lymph nodes. N=2 per group for non-tumour bearing lymph nodes.

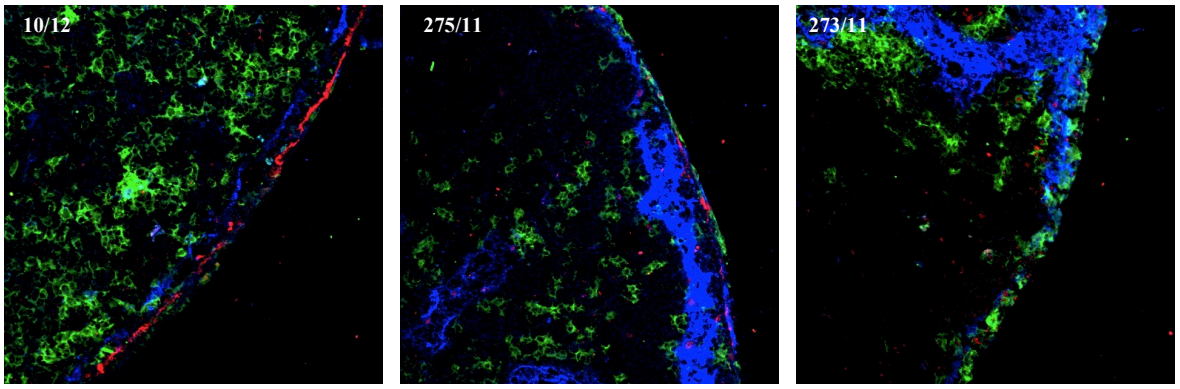

Figure 4.9: CCRL1 Expression is Downregulated in the Sinus of Tumour Bearing Lymph Node Sections.

Representative images of inguinal lymph node sections taken from WT and CCRL1-KO C57BL/6 mice. Mice received $1x10^5$ CCR7-expressing B16-F1 melanoma cells via subcutaneous injection. Mice were sacrificed after 3 weeks and serial lymph node sections cut and frozen. Frozen sections were fixed in 4% PFA for 10 minutes and stained for the presence of LYVE-1^+ lymphatic vessels (red), Langerin cells (green) and CCL21 (blue). Sections were then counterstained with DAPI and mounted using ProLong Gold. Images were taken at 25x magnification using the Zeiss LSM 510 confocal microscope. N=7 per group for WT lymph nodes. N=3 per group for CCRL1-KO lymph nodes.

a)

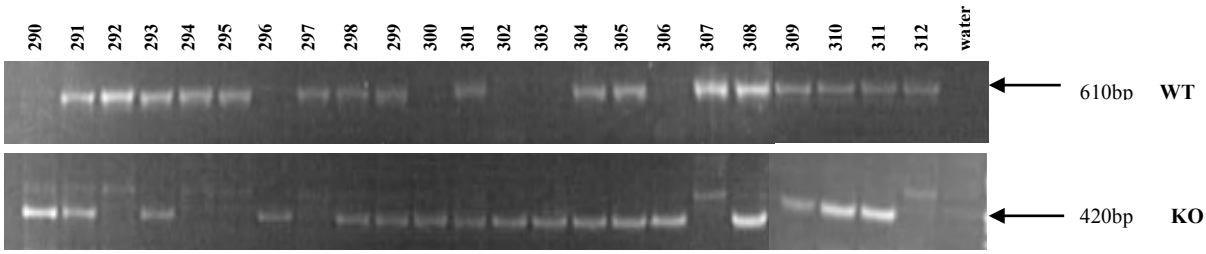

b)

Mouse Number	Genotype
290 *	-/-
291	+/-
292 *	+/+
293	+/-
294 *	+/+
295	+/+
296 *	-/-
297 *	+/+
298	+/-
299	+/-
300 *	-/-
301	+/-
302 *	-/-
303	-/-
304	+/-
305	+/-
306	-/-
307 *	+/+
308	+/-
309	+/-
310	+/-
311	+/-
312	-/-

Figure 4.10: PCR Genotyping of CCRL1 Genomic DNA.

PCR genotyping of ear-punch genomic DNA obtained from WT (+/+), CCRL1-heterozygous (+/-) and CCRL1-homozygous KO (-/-) mice. **a)** Ear-punch tissue was lysed using PCR lysis buffer at 95°C for 20 minutes. The lysis buffer was inactivated upon the addition of PCR neutralizing buffer and the lysed tissue was centrifuged briefly before being PCR amplified. PCR products were separated by agarose gel electrophoresis using a 1.5% agarose gel and visualized using SYBR safe DNA gel stain. **b)** Table summarising the genotype of each mouse. * = Mice selected for use in tumour experiment.

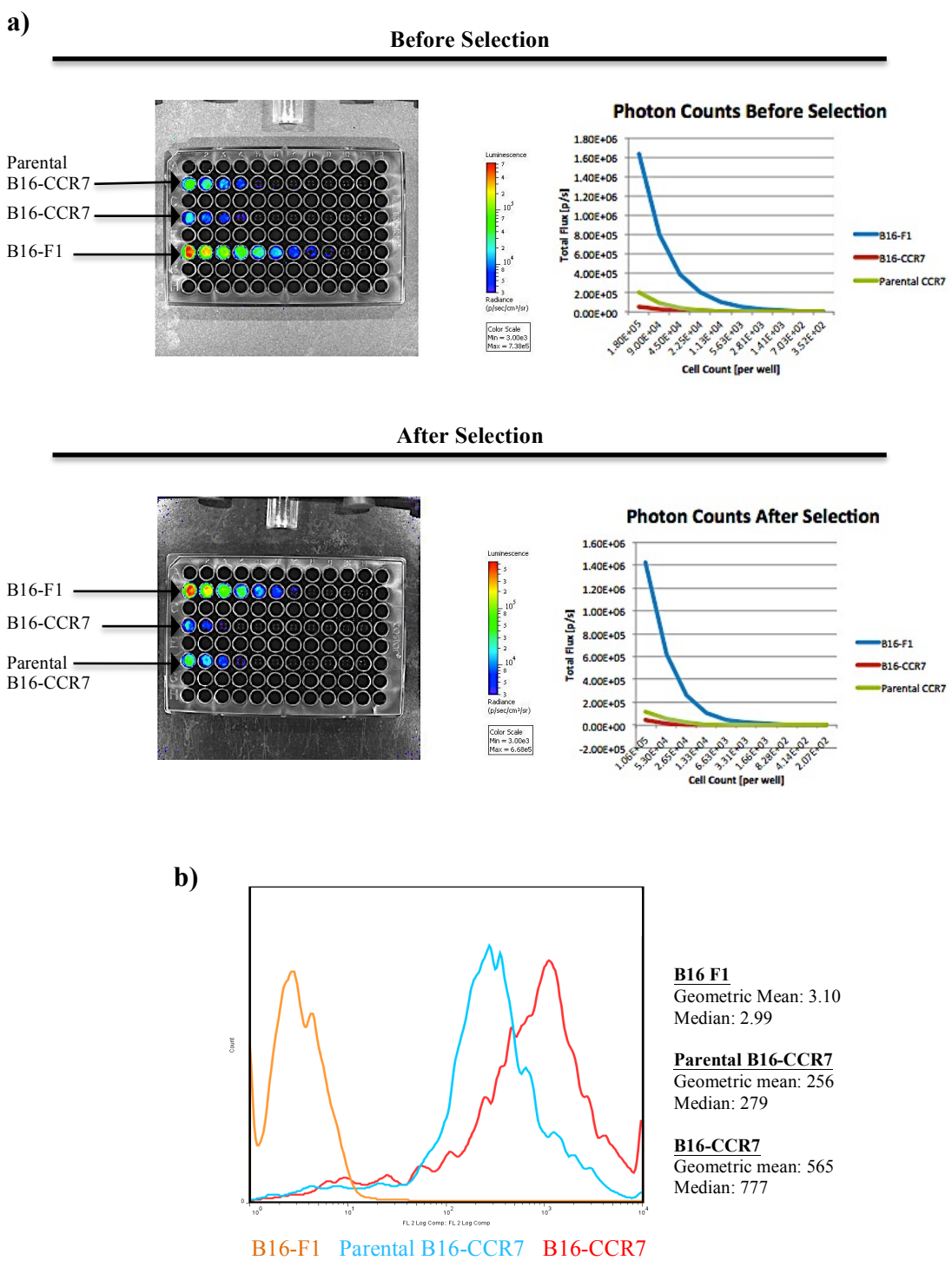

Figure 4.11: Optimisation of the Expression of Luciferase and CCR7 in the B16-CCR7 Cell Line.

a) Optimisation of luciferase expression in B16-CCR7 cells. Cells were seeded into a black-walled 96-well tissue culture plate at a 1:2 titration with a starting concentration of $1x10^5$ cells/well both before and after selection with puromycin. The cells were incubated overnight at 37°C. Prior to imaging, the media was aspirated and replaced with 100µl/well of D-Luciferin. The plates were imaged using the IVIS® Spectrum intravital microscope and analysed using the IVIS® Living Image software. Region-of-interest (ROI) measurements were generated using the IVIS® Living Image software and exported to Microsoft Excel. Graphs were generated by plotting the ROI values for each experimental condition against the cell count. **b)** Optimisation of CCR7 expression in B16-CCR7 cells. B16-F1, parental B16-CCR7 and geneticin-selected B16-CCR7 cells were seeded at $0.5x10^6$ cells/well in to a clear, round-bottomed 96-well plate and then Fc-blocked for 10 minutes at 4°C before being stained using a PE-conjugated anti-CCR7 antibody and near infrared cell death stain. Immunostained cells were analysed using the Beckman Coulter CyAn™ ADP analyser and FlowJo software. N=1

a)

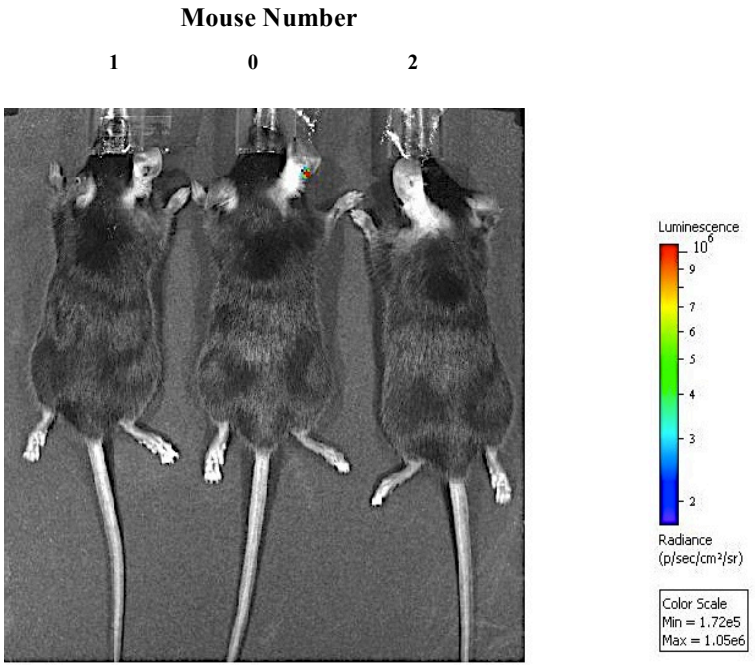

b)

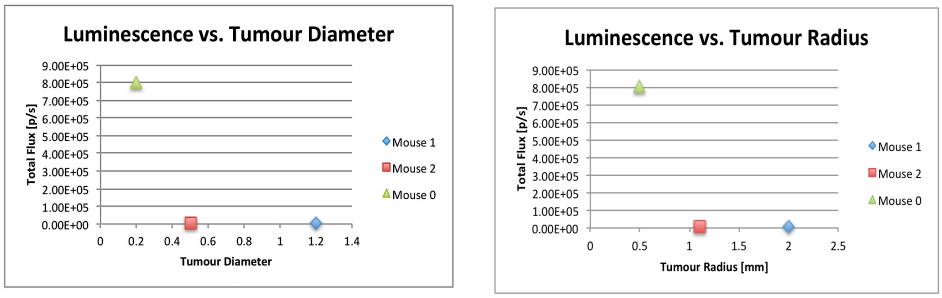

Figure 4.12: Expression of Luciferase by B16-CCR7 Cells Does Not Correlate With Tumour Size.

a) B16-F1 and B16-CCR7 cells were harvested by trypsinisation and resuspended at $60x10^6$ cells/ml in cold PBS. Cells were then passed through a 70µm strainer and the final concentration adjusted to $50x10^6$ cells/ml. For ear injections, 20µl of cell suspension was injected into the subcutaneous space under the central dorsal surface of the ears of both WT and CCRL1-KO C57BL/6 mice. Mice were weighed and received D-Luciferin via i.p. injection (10µl per kg body weight). After 5 minutes, the mice were anaesthetised with 2.5% isoflurane and then imaged using the IVIS® Spectrum intravital microscope. **b)** ROI measurements were generated using the IVIS® Living Image software and exported to Microsoft Excel. Tumour diameter and radius was also measured using a caliper and graphs generated by plotting the ROI values against tumour diameter or radius. N=1.

5. DISCUSSION

Metastasis is the major cause of death from cancer. It is a highly complex process and despite much progress, the molecular mechanisms underlying tumour metastasis remain elusive. As such, a better understanding of the mechanisms by which tumour cells traffic to secondary organs is warranted and may help inform the development of more targeted therapies to improve patient prognosis. In recent years, a role for chemokine receptors and their chemokine ligands in tumour growth, survival and metastasis has been suggested. Expression of CXCR4 and its cognate ligand CXCL12, for example, have been associated with enhanced migration and metastasis (33). Consistent with this, elevated CXCR4 expression has been demonstrated in breast tumours and their metastases (34). In addition, CCR7 has been found to be highly expressed in metastatic breast cancer (34).

CCR7 is primarily involved in regulating the homing of leukocytes to LNs. It also plays a prominent role in immune cell positioning within LNs. Mice deficient in CCR7 display a strong reduction in LN cellularity as a result of impaired T cell and DC migration (20,23). Immobilisation of its chemokine ligands, CCL19 and CCL21, on the apical surface of inflamed endothelium induces significant PBL arrest and transmigration, providing further evidence for CCR7-involvement in leukocyte homing (16).

Interestingly, the lymphatic invasion and subsequent migration of melanoma tumour cells towards the SLN bears many similarities with the normal trafficking of antigen-bearing DCs to regional draining LNs. Indeed, several lines of evidence exist that implicate CCR7 in metastasis to LNs (1,10,25-28). On the other hand, relatively little is known about the contribution of CCRL1 or how its expression affects the axis role

of CCR7-CCL19/21 in LN metastasis. In this present study, we investigated CCR7-driven metastasis and survival in the LN and examined whether host CCRL1 expression affects these processes.

Using the immunohistochemical staining method developed during initial experiments, we present the novel finding that CCR7-expressing B16 melanoma (B16-CCR7) preferentially establishes within the B cell areas of the LN. Individual B16-CCR7 cells were also identifiable within the sinus, however some were found to be both TRP-2^+ and $CD45^+$. These possibly represent activated DCs or macrophages that are presenting processed TRP-2 peptides on their surface. The significance of the above finding is not fully clear as the role of B cells in melanoma metastasis has not been extensively studied. It may be that the B cells provide survival factors or protection from the otherwise harsh environment of the LN. Large numbers of peritumoural B cells have been documented in primary melanoma (35). Furthermore, high B cell numbers were associated with a significant survival advantage (35).

Alternatively, B cells may impair T cell-mediated anti-tumour immune responses. Effector-memory and IFNγ or TNFα-secreting $CD4^+$ and $CD8^+$ T cell activation and Ag-specific $CD8^+$ T cell proliferation have been proposed to be impaired in tumour-bearing mice lacking mature B cells (36). Similarly, B cell-deficient mice display significant resistance to syngeneic B16 melanoma growth, as compared to WT mice (37); an observation thought to be a result of increased T_H1 cytokine release and induction of CTL responses (37). B cells may also promote tumour growth and survival by secreting B cell factors that induce chronic inflammation (38). Melanoma tumour establishment in the LN did not appear to be affected by depletion of CCRL1. Further experiments are required to gain a better understanding of the role of B cells in metastatic melanoma growth and survival in the LN. Depletion of B cells in both WT

and CCRL1-KO mice would provide detailed information about where, in the LN, these metastases, occur in the absence of B cells.

A number of $CD45^+$ $TRP\text{-}2^-$ cells were identified within the tumour foci. In an attempt to further characterise them, an array of antibodies raised against common immune cell markers were employed. A large number of $CD4^+$ cells were found to infiltrate the tumour – this was unchanged in CCRL1-KO mice. These could potentially be $CCR7^+$ lymphoid tissue inducer (LTi) cells. Previously published data has shown that $CD45^+CD3\varepsilon^-ROR\gamma t^+$ LTi cells are preferentially recruited to both WT and $CCL21^{high}$ melanoma tumours in a CCR7-dependant manner (39). Further, LTi recruitment was associated with enhanced tumour growth as depletion of LTi cells impeded melanoma tumour growth (39). Immunohistochemical staining for RORγt, in conjunction with CD45, CD3 and other known LTi markers, would be required to confirm this.

Further staining revealed that melanoma metastasis may suppress CCL21 and CCRL1 expression in the LN sinus. ACRs are believed to mediate the transcytosis of chemokines and their concentration at particular sites (17). Loss of CCRL1 may, therefore, result in reduced expression of CCL19 and CCL21 in the sinus. Downregulation of CCL21 at the sinus has been reported before (28) and could be a potential mechanism to suppress the recruitment of DCs and T cells. Of note, CCL21 was found to be present in the tumour. This is most likely CCL21-binding to the CCR7 receptors present on the tumour cells rather than secretion of CCL21 by the tumour cells, as they have been characterised as being $CCL21^-$. CCL21 has been reported to be present in melanoma tumours and is purported to be associated with the induction of an immunotolerant microenvironment(39). Further work would involve using more quantitative methods to analyse CCL21 and CCRL1 expression in the LN.

A possible method would involve laser capture microdissection (LCM) of the LN marginal sinus followed by Western blotting or PCR.

As the majority of LNs displayed well-established metastases, it was not possible to examine the kinetics of tumour growth and the effect of CCRL1 expression in early LN metastasis *in vivo*. In order to address this, B16-CCR7 cells were injected into the ears of WT and CCRL1-KO mice. Interestingly, WT mice developed primary tumours at the site of inoculation with delayed kinetics when compared with CCRL1-KO mice, suggesting that depletion of CCRL1 markedly enhances tumour growth. The size of the tumours were determined and mice were then imaged using the IVIS Spectrum® intravital microscope to evaluate the sensitivity of the B16-CCR7 cell line. Tumour size was found not to correlate with luciferase activity. A possible reason for the lack of luciferase activity in the largest of the tumours could be that this particular tumour had a much larger necrotic focus, with relatively few viable cells. Alternatively, the cell line might be heterogeneous in its expression of luciferase. Future work would, therefore, involve further optimisation of the cell line. Superinfection of the luciferase vector, followed by long-term antibiotic selection should be performed.

In summary, CCR7-expressing B16 melanoma preferentially establishes in the B cell areas of the LN and suppresses both CCL21 and CCRL1 expression in the marginal sinus, possibly to limit the recruitment of DCs and T cells. Depletion of CCRL1 did not appear to affect tumour growth and survival in the LN. CCRL1-deficient mice did, however, develop tumours with enhanced kinetics when compared to WT mice. Future work will help to further unravel the roles of CCR7 and CCRL1 in melanoma metastasis.

6. REFERENCES

(1) Wiley HE, Gonzalez EB, Maki W, Wu M, Hwang ST. Expression of CC chemokine receptor-7 and regional lymph node metastasis of B16 murine melanoma. J Natl Cancer Inst 2001;93(21):1638-1643.

(2) Watson M, Johnson CJ, Chen VW, Thomas CC, Weir HK, Sherman R, et al. Melanoma Surveillence In The Unites States: Overview Of Methods. JAAD 2011;65(5):S6.

(3) Skin Cancer Statistics-Key Facts. Available at: http://info.cancerresearchuk.org/cancerstats/keyfacts/skin-cancer/. Accessed June/24, 2012.

(4) Malignant Melanoma-One, Five And Ten-year Survival Rates. Available at: http://info.cancerresearchuk.org/cancerstats/types/skin/survival/. Accessed June/24, 2011.

(5) Eggermont A. Advances in systemic treatment of melanoma. Annals of Oncology 2010;21(suppl 7):vii339-vii344.

(6) Finn L, Markovic SN, Joseph RW. Therapy for metastatic melanoma: the past, present, and future. BMC Medicine 2012;10(1):23.

(7) Mehlen P, Puisieux A. Metastasis: a question of life or death. Nature Reviews Cancer 2006;6(6):449-458.

(8) Kakinuma T, Hwang ST. Chemokines, chemokine receptors, and cancer metastasis. J Leukoc Biol 2006;79(4):639-651.

(9) Chambers AF, Groom AC, MacDonald IC. Dissemination and growth of cancer cells in metastatic sites. Nature Reviews Cancer 2002;2:563-572.

(10) Emmett MS, Lanati S, DUNN D, Stone OA, Bates DO. CCR7 mediates directed growth of melanomas towards lymphatics. Microcirculation 2011;18(3):172-182.

(11) Shields J, Emmett M, Dunn D, Joory K, Sage L, Rigby H, et al. Chemokine-mediated migration of melanoma cells towards lymphatics–a mechanism contributing to metastasis. Oncogene 2006;26(21):2997-3005.

(12) Rot A, von Andrian UH. Chemokines in innate and adaptive host defense: basic chemokinese grammar for immune cells. Annu Rev Immunol 2004;22:891-928.

(13) Murakami T, Cardones AR, Hwang ST. Chemokine receptors and melanoma metastasis. J Dermatol Sci 2004;36(2):71-78.

(14) Ley K, Laudanna C, Cybulsky MI, Nourshargh S. Getting to the site of inflammation: the leukocyte adhesion cascade updated. Nature Reviews Immunology 2007;7(9):678-689.

(15) Johnson LA, Jackson DG. Inflammation-induced secretion of CCL21 in lymphatic endothelium is a key regulator of integrin-mediated dendritic cell transmigration. Int Immunol 2010;22(10):839-849.

(16) Cinamon G, Shinder V, Alon R. Shear forces promote lymphocyte migration across vascular endothelium bearing apical chemokines. Nat Immunol 2001;2(6):515-522.

(17) Ulvmar MH, Hub E, Rot A. Atypical chemokine receptors. Exp Cell Res 2011.

(18) Comerford I, Milasta S, Morrow V, Milligan G, Nibbs R. The chemokine receptor CCX□CKR mediates effective scavenging of CCL19 in vitro. Eur J Immunol 2006;36(7):1904-1916.

(19) Comerford I, Nibbs RJB, Litchfield W, Bunting M, Harata-Lee Y, Haylock-Jacobs S, et al. The atypical chemokine receptor CCX-CKR scavenges homeostatic chemokines in circulation and tissues and suppresses Th17 responses. Blood 2010;116(20):4130-4140.

(20) Förster R, Davalos-Misslitz AC, Rot A. CCR7 and its ligands: balancing immunity and tolerance. Nature Reviews Immunology 2008;8(5):362-371.

(21) Von Andrian UH, Mempel TR. Homing and cellular traffic in lymph nodes. Nature Reviews Immunology 2003;3(11):867-878.

(22) Saeki H, Moore AM, Brown MJ, Hwang ST. Cutting edge: secondary lymphoid-tissue chemokine (SLC) and CC chemokine receptor 7 (CCR7) participate in the emigration pathway of mature dendritic cells from the skin to regional lymph nodes. The Journal of Immunology 1999;162(5):2472-2475.

(23) Braun A, Worbs T, Moschovakis GL, Halle S, Hoffmann K, Bölter J, et al. Afferent lymph-derived T cells and DCs use different chemokine receptor CCR7-dependent routes for entry into the lymph node and intranodal migration. Nat Immunol 2011;12(9):879-887.

(24) Heinzel K, Benz C, Bleul CC. A silent chemokine receptor regulates steady-state leukocyte homing in vivo. Science's STKE 2007;104(20):8421.

(25) Fang L, Lee VC, Cha E, Zhang H, Hwang ST. CCR7 regulates B16 murine melanoma cell tumorigenesis in skin. Journal of Leukocyte Biology 2008 October 01;84(4):965-972.

(26) LIU FY, ZHAO ZJ, PENG L, DING X, GUO N, YANG LL, et al. NF-ϰB participates in chemokine receptor 7-mediated cell survival in metastatic squamous cell carcinoma of the head and neck. Oncol Rep 2011;25(2):383-391.

(27) Takeuchi H, Fujimoto A, Tanaka M, Yamano T, Hsueh E, Hoon DSB. CCL21 chemokine regulates chemokine receptor CCR7 bearing malignant melanoma cells. Clinical cancer research 2004;10(7):2351-2358.

(28) Takekoshi T, Fang L, Paragh G, Hwang S. CCR7-expressing B16 melanoma cells downregulate interferon-γ-mediated inflammation and increase lymphangiogenesis in the tumor microenvironment. Oncogenesis 2012;1(5):e9.

(29) Feng LY, Ou ZL, Wu FY, Shen ZZ, Shao ZM. Involvement of a novel chemokine decoy receptor CCX-CKR in breast cancer growth, metastasis and patient survival. Clinical cancer research 2009;15(9):2962-2970.

(30) Mahmood MN, Lee MW, Linden MD, Nathanson S, Hornyak TJ, Zarbo RJ. Diagnostic value of HMB-45 and anti-Melan A staining of sentinel lymph nodes with isolated positive cells. Modern pathology 2002;15(12):1288-1293.

(31) Kroumpouzos G, Urabe K, Kobayashi T, Sakai C, Hearing VJ. Functional-Analysis of the Slaty Gene-Product (TRP2) as Dopachrome Tautomerase and the Effect of a Point Mutation on Its Catalytic Function. Biochem Biophys Res Commun 1994;202(2):1060-1068.

(32) Kameyama K, Sakai C, Kuge S, NISHIYAMA S, Tomita Y, Ito S, et al. The Expression of Tyrosinase, Tyrosinase□Related Proteins 1 and 2 (TRP1 and TRP2), the Silver Protein, and a Melanogenic Inhibitor in Human Melanoma Cells of Differing Melanogenic Activities. Pigment cell research 1995;8(2):97-104.

(33) Kedrin D, van Rheenen J, Hernandez L, Condeelis J, Segall JE. Cell motility and cytoskeletal regulation in invasion and metastasis. J Mammary Gland Biol Neoplasia 2007;12(2):143-152.

(34) Müller A, Homey B, Soto H, Ge N, Catron D, Buchanan ME, et al. Involvement of chemokine receptors in breast cancer metastasis. Nature 2001;410(6824):50-56.

(35) Ladányi A, Kiss J, Mohos A, Somlai B, Liszkay G, Gilde K, et al. Prognostic impact of B-cell density in cutaneous melanoma. Cancer Immunology, Immunotherapy 2011:1-10.

(36) DiLillo DJ, Yanaba K, Tedder TF. B cells are required for optimal CD4 and CD8 T cell tumor immunity: therapeutic B cell depletion enhances B16 melanoma growth in mice. The Journal of Immunology 2010;184(7):4006.

(37) Shah S, Divekar AA, Hilchey SP, Cho HM, Newman CL, Shin SU, et al. Increased rejection of primary tumors in mice lacking B cells: Inhibition of anti□tumor CTL and TH1 cytokine responses by B cells. International journal of cancer 2005;117(4):574-586.

(38) De Visser KE, Korets LV, Coussens LM. De novo carcinogenesis promoted by chronic inflammation is B lymphocyte dependent. Cancer cell 2005;7(5):411-423.

(39) Shields JD, Kourtis IC, Tomei AA, Roberts JM, Swartz MA. Induction of lymphoidlike stroma and immune escape by tumors that express the chemokine CCL21. Science's STKE 2010;328(5979):749.

7. APPENDIX A: Information on CCRL1 Primers

Table 1. The Primer Sets Used for Genotyping.

Primer	Primer Sequence (5'-3')
11com5 (common)	TGC TGG TGA GCT CTG GGT TC
3IRES (knockout)	CCC TAG ATG CAT GCT CGA CG (homologous to sequence in the inserted construct)
11wt5 (wildtype)	AAT CGC CAC AAC TAC GGA GTT C

Does Rad6 Alter p53 Function Via Pituitary Tumour Transforming Gene 1 (PTTG1) – Binding Factor (PBF)?

By

Bhavika Modasia

13th August 2012

UNIVERSITY OF BIRMINGHAM

wellcome trust

ABSTRACT

Background: DNA damage checkpoints are essential for the suppression of genome instability, one of the main driving forces of tumour progression. The tumour suppressor, p53, is indispensible for the repair of damaged DNA and, as such, is tightly regulated. Pituitary tumour transforming gene 1 (PTTG1)-binding factor (PBF), a poorly characterised proto-oncogene, and Rad6, an E2 ubiquitin ligase, have both been reported to regulate p53 stability and function. Furthermore, Rad6 expression appears to be induced by overexpression of PBF.

Aims: The main objective was to investigate whether oncogenic levels of PBF promote p53 turnover through Rad6 activity. Further research involved determining whether Rad6 expression is altered in thyroid cancer.

Methods: Western blotting and Taqman RT-PCR were used to assess the level of PBF, Rad6 and p53 expression in thyroid cancer cell lines and in matched human normal and thyroid cancer specimens. Co-immunoprecipitation assays were performed to determine whether Rad6 and PBF physically interact.

Results: PBF directly binds to Rad6 and may regulate p53 stability and function via this interaction. In addition, Rad6 expression is induced in thyroid cancer and appears to positively correlate with PBF expression.

Discussion: The report demonstrates a potential mechanism by which PBF may be regulating p53 stability.

ACKNOWLEDGMENTS

Firstly I would like to thank my supervisor Professor Chris McCabe, for offering me the opportunity to carry out my project in his lab and for his endless support and encouragement. I am eternally grateful. I would also like to thank everyone in the McCabe group. In particular Gavin Ryan, for his invaluable assistance, technical support and patience and Martin Read for his much appreciated guidance.

ABBREVIATIONS

ATC – Anaplastic thyroid cancer

BCA – Bicinchoninic acid

DIT – Diiodotyrosine

E1- Ubiquitin-activating enzyme

E2 – Ubiquitin-conjugating enzyme

E3 – Ubiquitin-ligase

FTC – Follicular thyroid cancer

MDM2 – Mouse double minute protein 2

MIT – Monoiodotyrosine

NIS – Sodium iodide symporter

NLS – Nuclear localisation signal

PBF – PTTG-binding factor

PBF-Tg – transgenic mouse model of PBF overexpression

PCNA – Proliferating cell nuclear antigen

PTC – Papillary thyroid cancer

PTTG – Pituitary tumour transforming gene

T_3 – 3,5,3'-triiodothyronine

T_4 – Tetraiodothyronine

Tg – Thyroglobulin

UBE2A – Rad6A

UBE2B – Rad6B

WT – Wild-type

TABLE OF CONTENTS

LIST OF ILLUSTRATIONS

1. INTRODUCTION

1.1. The Thyroid Gland

The thyroid gland is a butterfly-shaped endocrine organ (figure 1.1). It is situated in the neck, anterior to the larynx and is composed of 2 lateral lobes connected by a narrow section, known as an isthmus(40). Histological examination reveals 3 distinctive features of the thyroid – thyroid follicles, thyroid follicular cells and parafollicular C cells(40). The follicles form the main structural component of the thyroid and consist of a single layer of follicular cells enclosing a colloid-filled cavity (containing the thyroid hormone precursor, thyroglobulin (Tg)). Parafollicular C cells are also present within this monolayer and are responsible for the production of calcitonin (40).

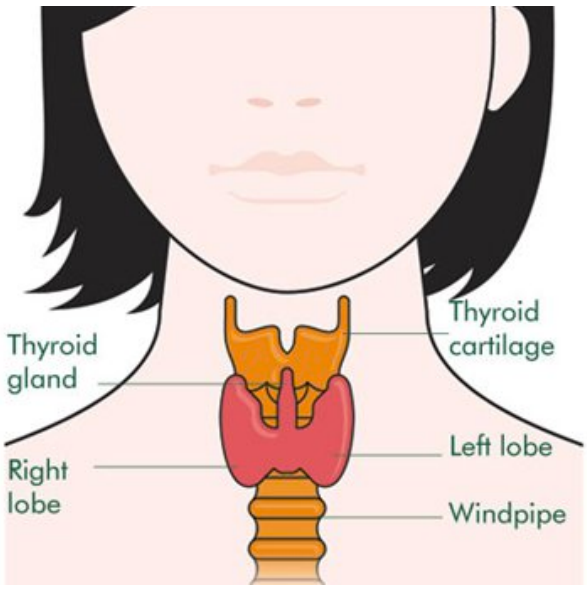

Figure 1.1: The Thyroid Gland

The thyroid gland is a butterfly-shaped organ. It is located at the back of the neck, anterior to the larynx. It is composed of two lateral lobes that are connected by an isthmus.

Figure taken from Macmillian Cancer Support, The Thyroid Gland – Cancer Information. Available at: http://www.macmillan.org.uk/Cancerinformation/Cancertypes/Thyroid/Aboutthyroidcancer/Thethyroidgland.aspx. Last updated 1st April 2010

The primary function of the thyroid is to produce and secrete the thyroid hormones,

tetraiodothyronine (T_4) and 3,5,3'-triiodothyronine (T_3). Synthesis of these hormones is primarily carried out by the follicular cells and is dependent on the presence of iodine, either obtained through the diet or via deiodinisation of T_4 in the bloodstream (40). Iodine is actively transported into the lumen by the sodium iodide symporter (NIS) and linked to tyrosine residues on Tg to generate the thyroid hormone precursors, monoiodotyrosine (MIT) and diiodotyrosine (DIT) (40). These iodinated tyrosine residues subsequently combine to form T_4 and T_3, which bind to intracellular receptors to modulate the transcription of a number of genes (40).

1.2. Thyroid Carcinoma

Thyroid carcinomas are one of the most common endocrine malignancies, accounting for approximately 1% of all human cancers (40). An estimated 213 000 cases were diagnosed worldwide in 2008 (41), and whilst uncommon, the annual incidence, particularly that of papillary thyroid cancer, appears to be on the rise (42,43). This, however, may reflect an increase in pathologic detection rather than a true increase in incidence (42).

Thyroid carcinomas are typically classified based upon their cellular origin. Carcinomas arising from thyroid follicular cells can be categorised as differentiated carcinomas or undifferentiated anaplastic thyroid carcinoma (ATC) (40,44). Both Follicular (FTC) and papillary (PTC) thyroid cancer are examples of differentiated carcinomas and they comprise almost 80% of diagnosed cases (40).

Near-total or complete thyroidectomy, followed by post-operative ^{131}I therapy constitutes the main treatment strategy (40). Although thyroid cancer is associated with a favourable prognosis, as demonstrated by a 10-year survival rate of 93% and 85% for PTC and FTC respectively (45), up to 35% of patients present with metastases and recurrent disease (45).

Instability in the genome is a characteristic feature of almost all human tumours and is necessary to facilitate the acquisition of the several mutations required for tumour initiation and progression. Indeed, thyroid cancer has been shown to display defects in genome maintenance and repair, for example, in the form of aneuploidy (46).

1.3. The Tumour Suppressor p53

The tumour suppressor protein, p53 is possibly one of the most critical 'cellular gatekeepers' owing to its function in regulating cellular responses to DNA damage. It is a sequence-specific transcription factor (47) and has been shown to transactivate a plethora of target genes via direct binding to upstream p53 response elements (47). These target genes encode for proteins that are involved in a diverse array of cellular responses, including cell cycle regulation, apoptosis, senescence, DNA repair and angiogenesis (47,48). Under normal conditions, the levels of p53 are maintained at a low basal state. By contrast, p53 stabilisation and activation is rapidly induced in response to aberrant growth, DNA damage and cellular stress (48).

Not surprisingly, dysregulation of p53 function has been implicated in the majority of human cancers and more than 50% of all malignancies are believed to harbour inactivating mutations of the p53 gene (48). Interestingly, p53 mutations have been reported to occur late in tumour progression (49,50). For example, such mutations are rarely observed in differentiated thyroid cancer but have been reported in approximately 55% of ATCs (44).

The stability of p53 is tightly regulated by post-translational modification, more specifically via ubiquitination by the ubiquitin-proteasome degradation pathway (47). Ubiquitination of a protein requires 3 distinct enzymes; a ubiquitin-activating enzyme (E1), a ubiquitin-conjugating enzyme (E2) and an E3 ubiquitin-ligase (E3) (51). Activation of ubiquitin is achieved through a covalent thioester bond with E1 (51).

The activated ubiquitin is then actively transferred to E2, which then acts in concert with E3 to attach the ubiquitin to one or more lysine residues on the target protein (51). Monoubiquitination is thought to regulate protein localisation and membrane transport (51). Further ubiquitination is required for the efficient recognition and subsequent proteasomal degradation of the target protein (51).

The E3 ligase, mouse double minute protein 2 (MDM2) is purported to be the key regulator of p53 turnover (47). Not only does it facilitate the ubiquitination and degradation of p53, but also sterically hinders the transactivation domain, which is required for p53 transcriptional activity (47). Recent evidence suggests that other proteins may also be involved in regulating p53 stability and degradation independently of MDM2 (51-54).

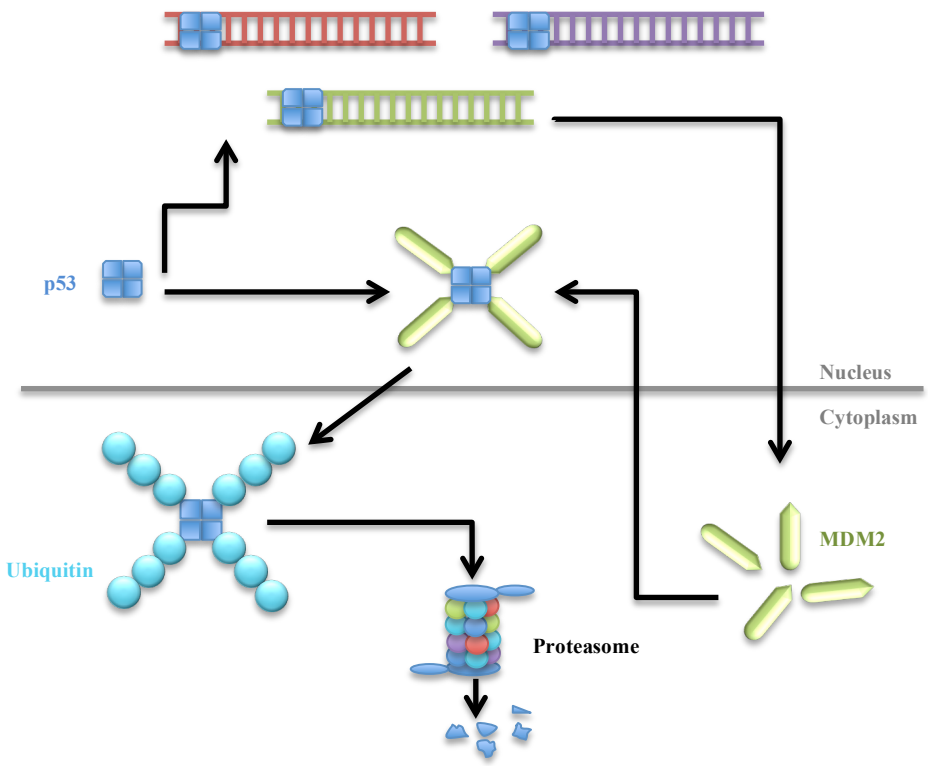

Figure 1.2: p53 Levels Are Regulated by MDM2

p53 levels rise in response to certain physiological stimuli (not shown) and bind to the promoter regions of a large number of target genes whose transcription it induces. One of the genes induced is MDM2 and this results in an increase in the level of MDM2 protein. MDM2 then binds to p53, which is exported from the nucleus and is ubiquitinated. Ubiquitination promotes the proteasomal degradation of p53. This negative feedback-loop ensures that p53 levels return to their usually low basal state.

1.4. PTTG1-Binding Factor

Pituitary tumour transforming gene 1 (PTTG1)-binding factor (PBF) is a poorly characterised protein that was initially discovered as a result of its ability to associate with the human securin, PTTG1 (55). The PBF gene is located within the chromosomal region 21q22.3 and encodes a 180 amino acid protein with a predicted molecular mass of 22 kDa (55). Of note, the peptide sequence appears to share no significant homology with any other human protein and is highly conserved across many animal species, thus signifying evolutionary importance and unique function (56). Initial evidence from protein prediction studies led to speculation that PBF was a

cell membrane glycoprotein, however, the subsequent identification of bipartite nuclear localisation signal (NLS) suggests that PBF may also represent a nuclear protein (55,56).

It is well established that expression of PBF is ubiquitous (55). Nevertheless, relatively little has been reported with regards to its function. It has previously been demonstrated to facilitate the nuclear transport of PTTG1 (55). PTTG1 is believed to function as a proto-oncogene, regulating diverse cellular processes, such as cell cycle progression and DNA repair (46). All functions ascribed to PTTG1 require nuclear localisation; in this context PBF may play an indirect role in tumourigenesis (55). Recent evidence suggests that PBF may also be directly implicated in tumourigenesis as subcutaneous expression induces the formation of tumours in nude athymic mice (57). In support of this, altered PBF expression has been noted in a number of cancers, particularly that of the thyroid (56-59). In breast cancer, PBF overexpression and secretion was found to induce cell invasion (58). Several studies have also highlighted a role of PBF in sodium iodide symporter (NIS) regulation in the thyroid (60,61). Overexpression of PBF resulted in repression of NIS function, both *in vitro* and *in vivo* and induced significant hyperplasia within the thyroid (56,60-62). When taken together, these observations suggest PBF is a multifunctional proto-oncogene. However, the precise contribution of PBF in tumourigenesis remains elusive.

Recently, PBF has been identified as a novel regulator of p53 function (54). Oncogenic levels of PBF were found to induce a significant reduction in the half-life of p53, a finding that was correlated with increased p53 ubiquitination and repression of p53-mediated gene transactivation (54). Subsequent co-immunoprecipitation assays confirmed a direct interaction between PBF and p53(54). Consistent with this, p53 function was impaired in a transgenic mouse model of PBF overexpression (PBF-Tg)

(54). Gross genetic instability was also evident in PBF-Tg mice, as indicated by elevated levels of DNA repair genes, such as Rad6(54). Further, PBF, p53 and Rad6 expression were altered in matched human colorectal tumours, with p53 expression negatively correlating with both PBF and Rad6 expression(54).

1.5. The E2 Ubiquitin-Conjugating Enzyme, Rad6

Rad6 belongs to a group of E2 ubiquitin-conjugating enzymes primarily involved in DNA damage repair(63). In humans, the Rad6 gene is duplicated and, as a result, encodes for 2 proteins – Rad6A and Rad6B (95% sequence homology) (63). Both genes are highly conserved among eukaryotes and are known to be expressed in all tissues of the body(63). Rad6 interacts with 3 different E3 ubiquitin ligases in order to carry out the numerous functions ascribed(64). For example, association with Ubr1 promotes the degradation of target proteins through the N-end rule(64). Alternatively, the formation of a Rad6-Rad18 heterodimeric complex results in the ubiquitination of proliferating cell nuclear antigen (PCNA), which mediates post-replication DNA repair(64). Rad6 may also interact with Bre1, and potentially Lge1, to regulate gene transcription(65) through ubiquitination of the histone protein, H2B(66).

There is a growing body of evidence to suggest that Rad6 may also be implicated in the initiation and progression of many cancers. For example, overexpression has previously been documented in breast cancer (67). Rad6 has also been implicated in the regulation of p53 stability and function (52,53). In support of this, Rad6 has been shown to physically interact with p53 (51). As both PBF and Rad6 expression has been negatively correlated with p53 expression and both proteins have been reported to independently regulate p53 levels, it will be important to determine whether PBF overexpression influences p53 turnover by modulating Rad6 activity.

2. MATERIALS AND METHODS

2.1. Materials

Cell Lines

- K1 human papillary thyroid carcinoma cell line acquired from the Health Protection Agency Culture Collections (HPACC).
- TPC-1 human papillary thyroid carcinoma cell line obtained from Dr Rebecca Schweppe, University of Colorado, US.

Human Tissue

Matched normal and thyroid tumour tissue (N=11) was obtained from patients undergoing surgery at the University of Birmingham Queen Elizabeth Hospital, UK and stored at -80°C. Normal specimens were taken from the contralateral lobe at the time of surgery and were shown to be non-cancerous upon histological examination. All tissue samples were collected following local ethical approval and signed informed patient consent in accordance with the Declaration of Helsinki. Of the 11 tissue samples, there were 9 cases of papillary carcinoma and 2 cases of follicular carcinoma.

Cell Culture

- RPMI 1640 (- L-Glutamine) – Sigma-Aldrich, UK
- Opti-MEM reduced serum media – Gibco, UK

Antibodies

- Rabbit polyclonal antibody to Rad6 – Abcam #Ab31917
- Rabbit anti-human IGF-1 IgG – Biovision #5119-100
- Polyclonal goat anti-rabbit IgG-HRP – Dako #P0448

- Polyclonal rabbit anti-mouse IgG-HRP – Dako #P0161
- Mouse anti-β Actin – Sigma, UK #A3854
- Rabbit anti-human PBF antibody – made in-house
- P53 (DO-I) mouse monoclonal antibody IgG2a – Santa Cruz Biotechnology #SC-126
- Mouse anti-fibrillarin 38F3 IgG – Abcam #Ab4566

Taqman Gene Expression Assays

- Human PTTG1IP gene expression assay – Applied Biosystems #4351372
- Human UBE2A gene expression assay – Applied Biosystems #4331182
- QuantumRNA™ classic 18S internal standard – Applied Biosystems #AM1716M

Buffers and Solutions

- **Blocking Solution**: 5% w/v milk powder in TBST
- **TBST**: 1M tris pH 7.6, 5mM sodium chloride, tween-80 and dH_20
- **RIPA Lysis Buffer**: tris-HCl pH 7.4, sodium chloride, igepal, 10% sodium deoxycholate, 100mM EDTA and dH_20
- **Gel Sample Buffer**: 10% w/v DTT in laemlli buffer
- **5% Stacking Gel**: 0.8M tris-HCl pH6.8, 40% polyacrylamide, 10% SDS, 10% APS, TEMED and dH_20
- **12% Resolving Gel**: 1.5M tris-HCl pH8.8, 40% polyacrylamide, 10% SDS, 10% APS, TEMED and dH_20
- **10x Running Buffer**: tris base, glycine, SDS and dH_20. Dilute to 1x in dH_20
- **Transfer Buffer**: tris base, glycine, methanol, SDS and dH_20

Additional Materials

- Penecillin-streptomycin – Gibco, UK #15070-063
- DL-Dithiothreitol (DTT) – Sigma, UK #D9779-10G
- Phosphate buffered saline (PBS) tablets – Sigma, UK #P4417-100TAB
- Tween-80 – Sigma, UK #P4780
- Protogel – National Diagnostics, US - #EC-891
- Methanol – VWR, UK #20847.307
- Trypsin/EDTA – Invitrogen, UK #15400-054
- UBE2B silencer® select siRNA – Ambion, UK #4390824
- UBE2A silencer® select siRNA – Ambion, UK #4390825
- Silencer® negative control siRNA – Ambion, UK #AM4635
- Lipofectamine™ 2000 reagent – Invitrogen, UK #52887
- FuGene®6 transfection reagent – Roche, UK #11988387001
- Human UBE2A pCMV-XL5 cDNA clone – OriGene, US #SC109859.
- Precision plus protein dual colour standards – Biorad, US #161-0374
- Laemmli sample buffer – Biorad, US #161-0737
- Amersham ECL plus western blotting detection system – GE Life Sciences, UK #RPN2132
- Pierce® ECL2 western blotting substrate – Thermo Scientific, UK #P180197
- Trizma base – Sigma, UK #T1503
- Glycine – Sigma, UK #G8898
- TEMED – Sigma, UK #T9281
- Sodium chloride – Fischer Scientific, UK #S/3160/65
- Medical X-ray film – Kodak, US #8143059

- Sodium dodecyl sulphate (SDS) – Sigma, UK #L4390
- Ammonium persulphate (APS) – Sigma, UK #A3678
- Pierce® BCA assay – Thermo Scientific, UK #23227
- RNeasy mini kit – Qiagen, US #74104
- 2x GoldStar TaqMan PCR mastermix – Eurogentec, US #RT-QP2X-03+QGS
- Reverse transcription system – Promega, US #A3500
- AMV reverse transcriptase – IBR Stores, UK #M9004
- Random primers – IBR Stores, UK #C1181
- Protease inhibitor cocktail – Sigma, UK #P8340
- Foetal Calf Serum – Sigma, UK #10437-028
- Amersham Hybond P PVDF membrane – GE Life Sciences, UK #RPN303F
- Protein-G sepharose 4 fast flow – GE Life Sciences, UK #17-0618-01

2.2. Methods

2.2.1. Cell Culture

TPC-1 and K1 cells were routinely cultured in RPMI 1640 media supplemented with 10% FCS, penicillin and streptomycin. Cell cultures were incubated at 37°C in a humidified atmosphere containing 5% CO_2 until confluent. Cells were then detached using 0.25% trypsin/EDTA for 5 minutes at 37°C and harvested in 10-20ml of complete media. For transfection experiments, K1 cells were seeded at $1x10^5$ cells per well and TPC-1 cells at $7.5x10^4$ cells per well into clear, 6-well tissue culture plates. For co-immunoprecipitation, K1 and TPC-1 cells were seeded at $2.5x10^5$ cells and $1.875x10^4$ cells, respectively, in 5ml into vented $25cm^3$ tissue culture flasks. For routine cell culture maintenance, a 1:10 (K1) or 1:20

(TPC-1) dilution was carried out and the appropriate volume of cell suspension transferred to a vented 75cm^3 tissue culture flask containing pre-warmed media.

2.2.2. Transient Transfection of K1 and TPC-1 Cells

2.2.2.1. siRNA-induced Knockdown

K1 and TPC-1 cells seeded onto 6-well tissue culture plates were left to adhere overnight at 37°C in a CO_2 incubator. Cells were then transfected with either UBE2A+B siRNA or negative control siRNA at an optimal siRNA: Lipofectamine™ ratio of 1µl siRNA to 6µl of Lipofectamine™. Prior to transfection, Lipofectamine™ was diluted in opti-MEM and incubated at room temperature for 5 minutes. After the 5-minute incubation, the siRNA (40nM) was combined with the diluted Lipofectamine™ and incubated for a further 20 minutes to enable complex formation. The media was then aspirated from the wells of each tissue culture plate and replaced with 1ml/well of the transfection mix, after which, the cells were incubated at 37°C in a CO_2 incubator for 48 hours. The media was replaced with complete growth media 4-6 hours post-transfection.

2.2.2.2. Overexpression

K1 and TPC-1 cells seeded in 6-well tissue culture plates were left to adhere overnight at 37°C + 5% CO_2. The cells were then transfected using the Fugene® 6 transfection reagent according to the manufacturer's protocol. The optimal Fugene:DNA ratio was determined to be 3µl Fugene® per 1µg of plasmid DNA. Preparation of the complex involved diluting the Fugene® in opti-MEM and allowing the mixture to incubate at room temperature for 5 minutes. The plasmid DNA (2µg per well) was added to the mixture and left to incubate at room temperature for 20 minutes. 100µl of this transfection mix was then added in a drop-wise manner to each well, after which the plates were left to incubate for 48

hours at 37°C in a CO_2 incubator. For transfection of 25cm^3 tissue culture flasks, 250µl of the transfection mix was added to each flask (5µg plasmid DNA per flask).

2.2.3. Protein Extraction

Whole cell lysates were harvested in 250µl/well of RIPA lysis buffer containing protease inhibitors after a 20-mintue incubation at -20°C. Prior to loading, the protein concentration was measured by the Bicinchoninic acid (BCA) assay, using bovine serum albumin (BSA) as a standard. Lysates were then diluted to the appropriate concentration and solubilised using laemlli buffer containing 10% DTT at 95°C for 5 minutes. Samples were used immediately or stored at -20°C.

2.2.4. Western Blotting

Western blot analysis was performed by SDS-PAGE. Soluble protein samples were loaded onto 12% SDS-polyacrylamide gels, alongside a molecular weight marker, and electrophoresed at 140V. Once the proteins were fully separated, the gels were placed with PVDF membrane in a blot cassette, which was then run at 360mA for approximately 75 minutes to allow transfer of the proteins to the PVDF membrane. The membranes were incubated at room temperature in 5% milk in TBST for 1 hour with gentle shaking and followed by an overnight incubation with the primary antibody diluted in 5% milk in TBST at 4°C with gentle shaking. The membranes were washed 3 times with TBST for 10 minutes before incubation with the secondary antibody diluted in 5% milk in TBST for 1 hour at room temperature. The membranes were again washed 3 times in TBST for 10 minutes and developed by treatment with ECL plus followed by exposure on x-ray film. The x-ray film was developed using the Xograph Compact X4 x-ray film processor.

2.2.5. Co-immunoprecipitation Assays

K1 and TPC-1 cells transiently transfected with either pcDNA3 (vector only), PBF or UBE2A were harvested in 350µl of RIPA buffer containing protease inhibitors. After a brief sonication, cell lysates were centrifuged at 12000G for 10 minutes at 4°C. The lysate was transferred to a clean eppendorf and 35µl removed for use as a whole cell lysate sample. Each lysate was incubated with 30µl of beads prepared from protein-G sepharose 4 fast flow for 2 hours at 4°C with rotation. The lysates were then pulse centrifuged at 6000rpm for 30 seconds and the supernatant transferred to a clean eppendorf. Each lysate was incubated with 15µl of rabbit anti-PBF antibody or mouse anti-p53 antibody at 4°C overnight with rotation. Control samples were incubated without antibody, with a rabbit anti-IGF1 antibody or a mouse anti-fibrillarin antibody. The samples were further incubated with 30µl of bead slurry prepared from protein-G sepharose 4 fast flow beads for 3-4 hours at 4°C with rotation. The sepharose beads were then pulse centrifuged to remove any unbound protein and washed a further 6 times in 500µl of RIPA buffer. Any bound protein was then eluted in 30µl of laemmli buffer containing 1% SDS and 5% 2-β mercaptoethanol at 37°C for 30 minutes. The proteins were separated by SDS-PAGE following the western blotting protocol outlined above (ref: 3.2.4. Western Blotting).

2.2.6. Protein and RNA Extraction From Matched Normal and Tumour Tissue

Whole cell protein extracts from matched normal and thyroid cancer tissues were prepared in RIPA buffer containing protease inhibitors using a rotor-stator homogeniser. The protein concentration for each sample was determined by BCA assay, using BSA as a standard. Samples were then diluted to the appropriate

concentration before being separated by SDS-PAGE, as described previously (ref: 3.2.3. Protein Extraction and 3.2.4. Western Blotting).

Total RNA was extracted from the tissues using the RNeasy Mini kit (Qiagen), following the manufacturer's guidelines. The RNA was reverse transcribed using the avian myeloblastosis virus (AMV) Reverse Transcription System (Promega). Firstly, 0.5µg of total RNA was diluted in RNase-free water and incubated at 70°C for 10 minutes. A reverse transcription master mix was then prepared and combined with each RNA sample before being incubated for a further 10 minutes at room temperature. The samples were then PCR amplified (42°C – 1 hour, 95°C – 5 minutes, 4°C – 5 minutes), pulse spun and stored at -20°C after the addition of 10µl of RNase-free water.

2.2.7. Quantitative PCR

The expression of PBF and UBE2A mRNA was determined by quantitative PCR using the ABI PRISM 7700 Sequence Detection System. The PCR reaction was conducted in 96-well PCR plates. A 1µl aliquot of each cDNA sample was added to a 24µl master mix containing 2x TaqMan universal PCR master mix, a TaqMan gene expression assay (PBF/UBE2A or 18S) and RNase-free water, giving a total reaction volume of 25µl. The target gene probes were labelled with FAM and the 18S rRNA probe with VIC. The PCR reaction was as follows:

1. 50°C – 2 minutes
2. 95°C – 10 minutes
3. Then 40 cycles of 95°C for 15 seconds
4. 60°C – 1 minute

2.2.8. Data Analysis

Data are displayed as mean ± SEM. Normally distributed data was statistically analysed using a two-tailed Student's t-test unless otherwise stated. A *P* value of <0.05 was considered to be statistically significant.

3. AIMS AND OBJECTIVES

The main objective was to investigate whether oncogenic levels of PBF promote Rad6-mediated p53 turnover in the papillary thyroid cancer cells, K1 and TPC-1. Further research involved characterising Rad6 expression in human matched normal and thyroid cancer specimens, in conjunction with PBF and p53 expression.

4. RESULTS

4.1. Rad6 Appears to Regulate the Expression of PBF and p53 in K1 and TPC-1 Cells

To determine the relationship between Rad6, PBF and p53, we first assessed the effect of Rad6 overexpression on PBF and p53 protein expression. These experiments were performed in 2 human papillary thyroid cancer cell lines, K1 and TPC-1, both of which express WT p53. As shown in figure 4.1, transient transfection of K1 cells with Rad6 resulted in a reduction in endogenous expression levels of p53 and a marginal decrease in PBF expression, when compared to control-transfected cells. In contrast, depletion of Rad6 expression by siRNA was associated with increased expression of endogenous PBF (data not shown) and p53. Similar results were also observed in TPC-1 cells, although depletion of Rad6 appeared to result in reduced levels of p53 protein (figure 4.2). These results suggested that Rad6 may potentially be involved in the regulation of both PBF and p53 protein expression.

4.2. Co-Immunoprecipitation of Rad6 by p53 and PBF *In Vitro*

To further investigate an association between PBF and Rad6, endogenous co-immunoprecipitation experiments were performed using protein lysates prepared from TPC-1 cells transfected with PBF, Rad6 or empty vector. Consistent with previous findings(53), co-immunoprecipitation with an anti-p53 antibody revealed that Rad6 specifically interacts with p53 (figure 4.3). In addition, further co-immunoprecipitation assays using an anti-PBF antibody revealed a novel interaction between Rad6 and PBF (Figure 4.4). After immunoprecipitation of endogenous PBF, a band corresponding to Rad6 was detectable in lysates from Rad6-transfected cells but

not in cells transfected with PBF. This provided further support for a role of Rad6 in PBF regulation of p53 and raised the question of whether Rad6 levels were altered in cancer, as has been noted for PBF and p53.

4.3. Correlation Between Rad6 and PBF mRNA Expression in Matched Normal and Thyroid Cancer Tissue

Although PBF overexpression has been demonstrated in a number of cancers (56-59), Rad6 induction has only been documented in breast and colorectal cancer (54,67). Matched human normal and thyroid cancer specimens were therefore analysed to determine the endogenous expression levels of Rad6. The samples were also assessed for PBF and p53 expression to determine if there was any correlation with Rad6 expression *in vivo*.

Protein expression was quantified by western blotting (figure 4.5b). However, due to technical issues, β-actin expression could not be quantified. Protein concentrations were calculated twice, in triplicate, using the BCA assay and the BSA protein standards appeared to be accurate as demonstrated in figure 4.5a. Furthermore, coommassie staining of the PVDF membranes confirmed equal protein loading (not shown). 9/11 (82%) tumours demonstrated induced PBF expression (figure 4.5b), with a ~3-fold induction compared to matched normals (figure 4.6, P=0.02). 7/11 (64%) tumours also displayed upregulation of Rad6 expression (figure 4.5b), with a ~1.8 fold induction compared to matched normals (figure 4.6, P=0.02). p53 was present at high levels in 1 of 11 tumours and at lower levels in 6 others (figure 4.5b).

Rad6 and PBF mRNA expression was also examined in these samples by Taqman RT-PCR. A similar, albeit, non-significant trend was observed, with tumours demonstrating a ~2-fold increase in Rad6 mRNA expression and a ~1.4-fold increase in PBF mRNA expression (figure 4.7a). In addition, a significant positive correlation

was identified between PBF and Rad6 mRNA expression (figure 4.7b/c, r_s=0.9). In summary, the results show that Rad6 physically interacts with PBF, suggesting the possible involvement of Rad6 in PBF regulation of p53 function. In addition, Rad6 expression is induced in thyroid cancer and seems to correlate with PBF expression.

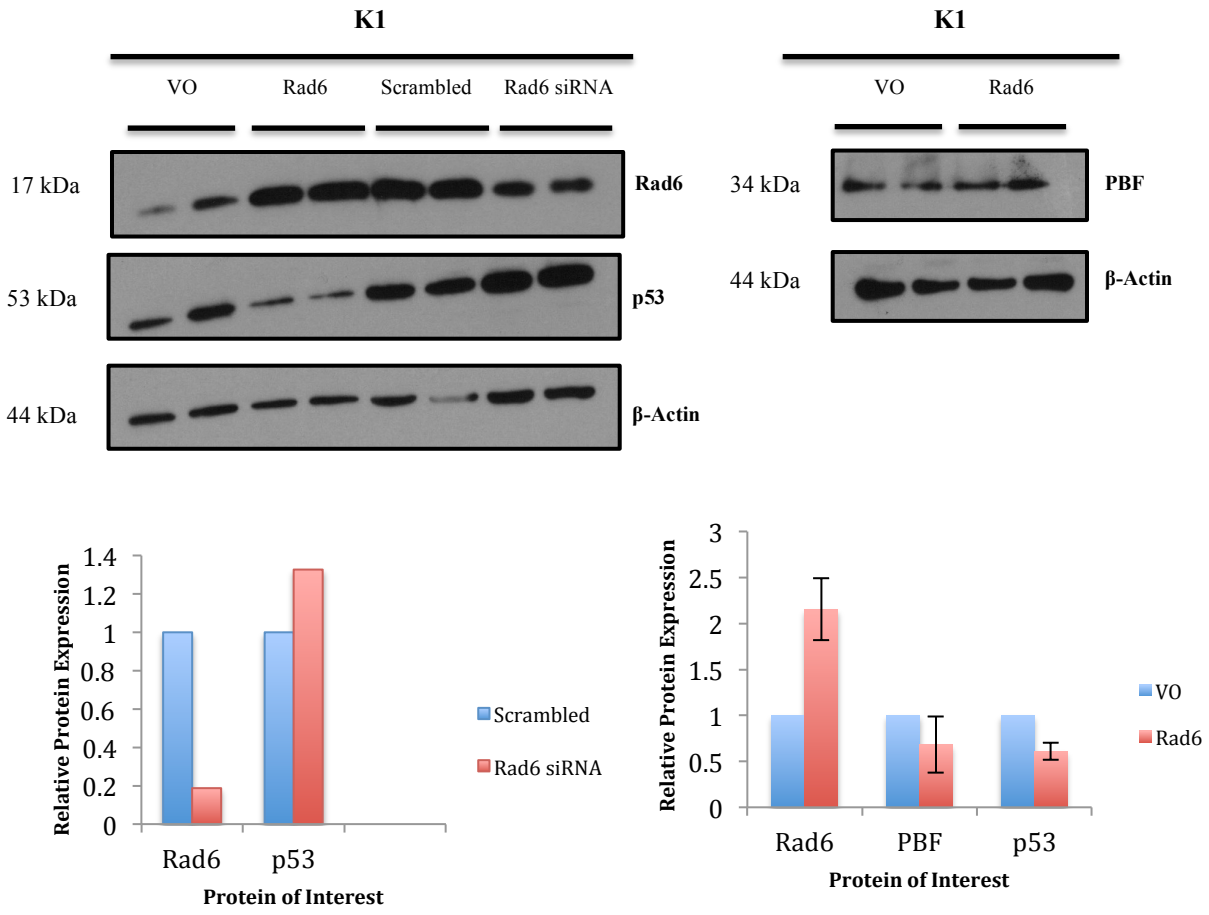

Figure 4.1: Rad6 Appears to Regulate the Expression of PBF and p53 in K1 Cells

K1 cells, plated at $1x10^5$ cells per well, were transfected with the indicated vectors or siRNAs and incubated at 24h or 48h, respectively. Whole cell lysates were then harvested and analysed by Western blotting with the indicated antibodies. The intensities of Rad6, p53 and PBF were quantified and the expression levels relative to β-actin are shown. Mean ± SEM. n=1 for Rad6 knockdown. n=2 for Rad6 overexpression.

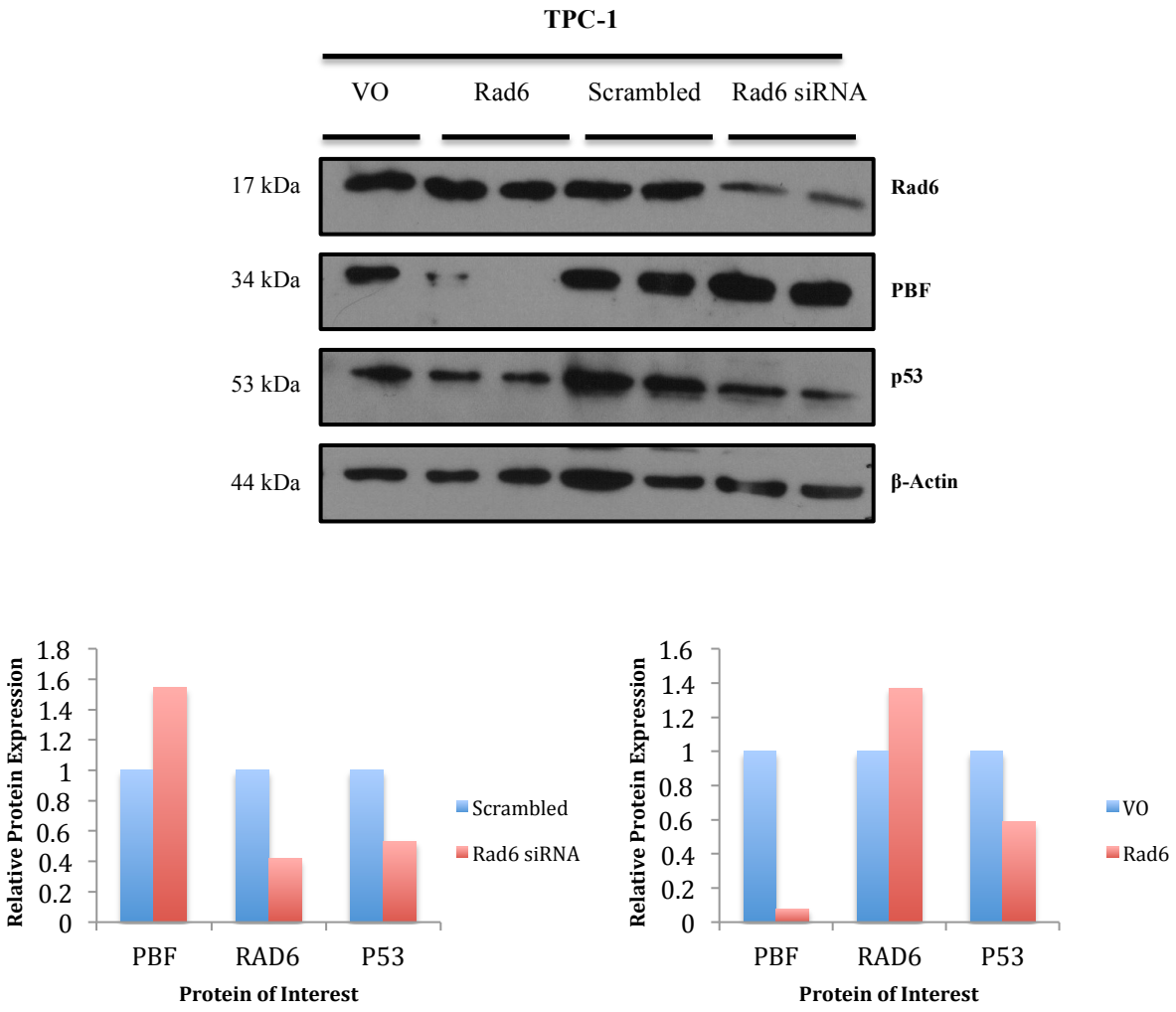

Figure 4.2: Rad6 Appears to Regulate the Expression of PBF and p53 in TPC-1 Cells

TPC-1 cells, plated at $7.5x10^4$ cells per well, were transfected with the indicated vectors or siRNAs and incubated at 24h or 48h, respectively. Whole cell lysates were then harvested and analysed by western blotting with the indicated antibodies. The intensities of Rad6, p53 and PBF were quantified and the expression levels relative to β-actin are shown. Mean ± SEM. n=1

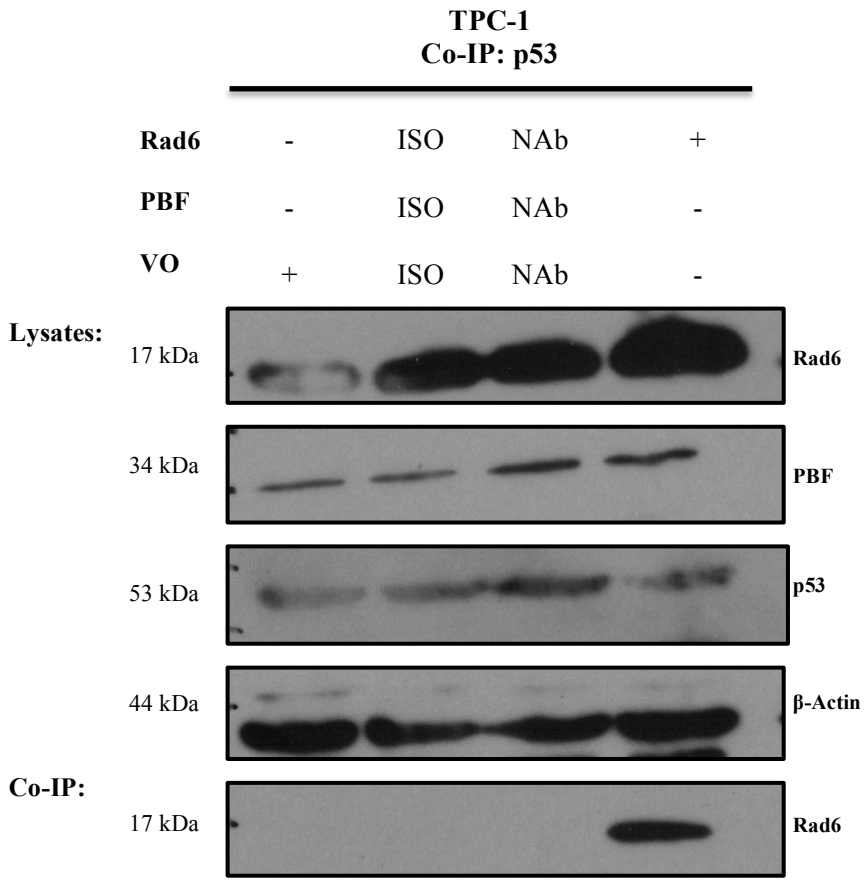

Figure 4.3: Co-Immunoprecipitation of Rad6 by p53 *in vitro*

TPC-1 cells were transfected with the indicated vectors and incubated for 48h. Whole cell lysates were then harvested and were subjected to co-immunoprecipitation of Rad6 with an anti-p53 antibody. Bound Rad6 was analysed by western blotting with an anti-Rad6 antibody. (-): no transfection, (+): transfection, NAb: no antibody control, ISO: isotype control. n=2

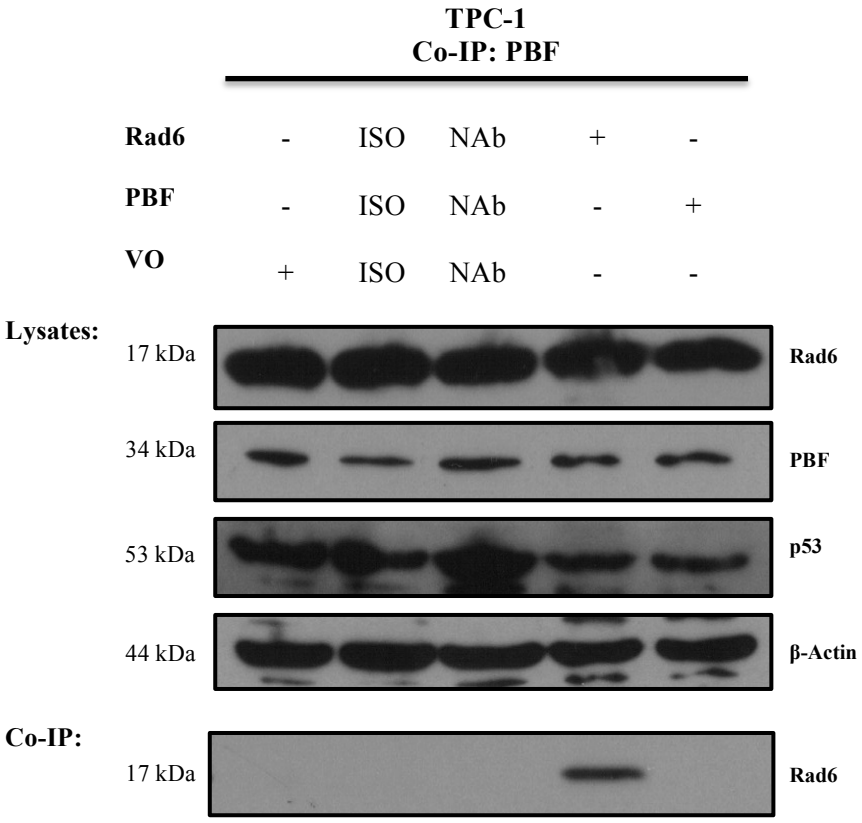

Figure 4.4: Co-Immunoprecipitation of Rad6 by PBF *in vitro*

TPC-1 cells were transfected with the indicated vectors and incubated for 48h. Whole cell lysates were then harvested and were subjected to co-immunoprecipitation of Rad6 with an anti-p53 antibody. Bound Rad6 was analysed by western blotting with an anti-Rad6 antibody. (-): no transfection, (+): transfection, NAb: no antibody control, ISO: isotype control. n=2

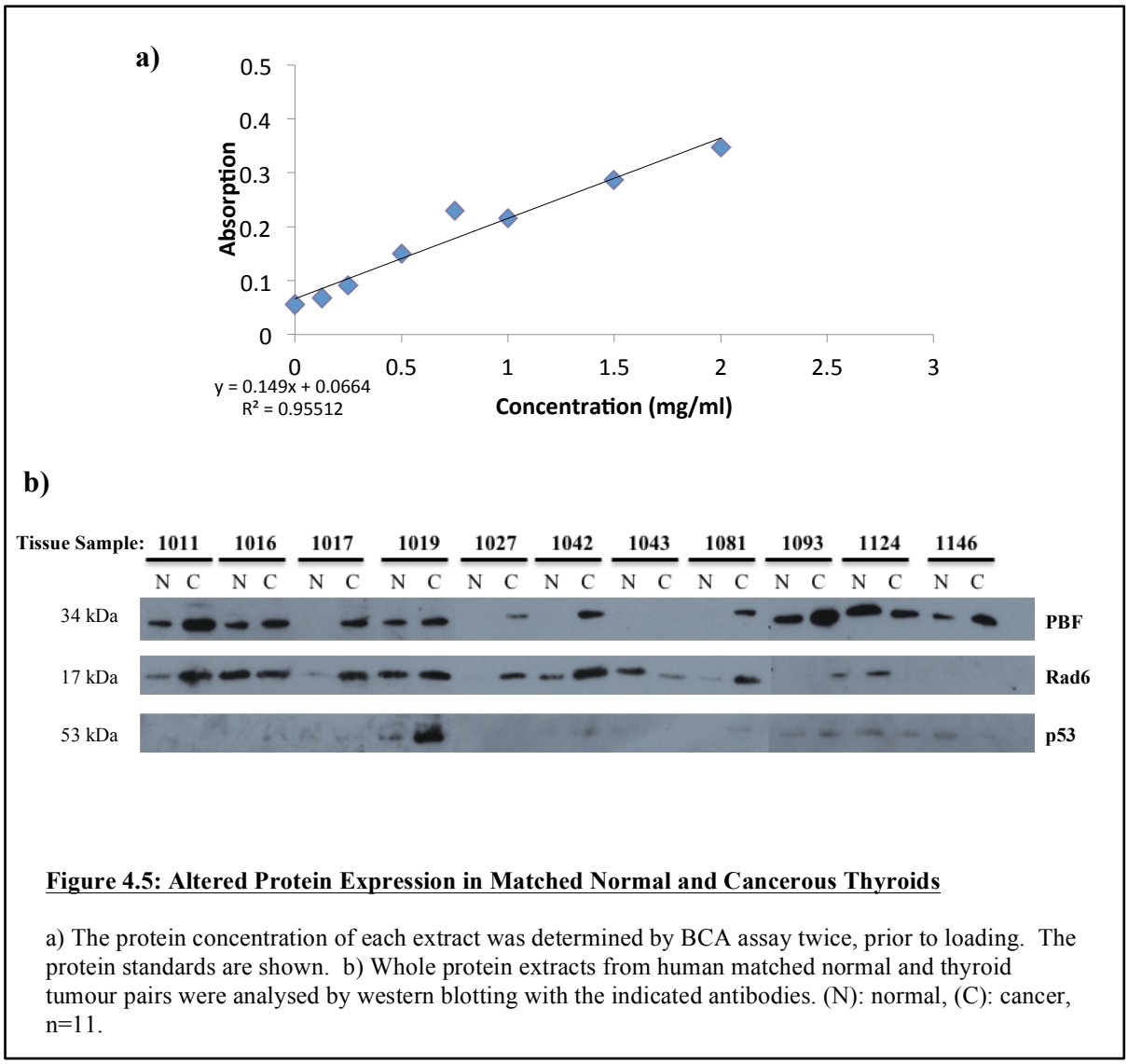

Figure 4.5: Altered Protein Expression in Matched Normal and Cancerous Thyroids

a) The protein concentration of each extract was determined by BCA assay twice, prior to loading. The protein standards are shown. b) Whole protein extracts from human matched normal and thyroid tumour pairs were analysed by western blotting with the indicated antibodies. (N): normal, (C): cancer, n=11.

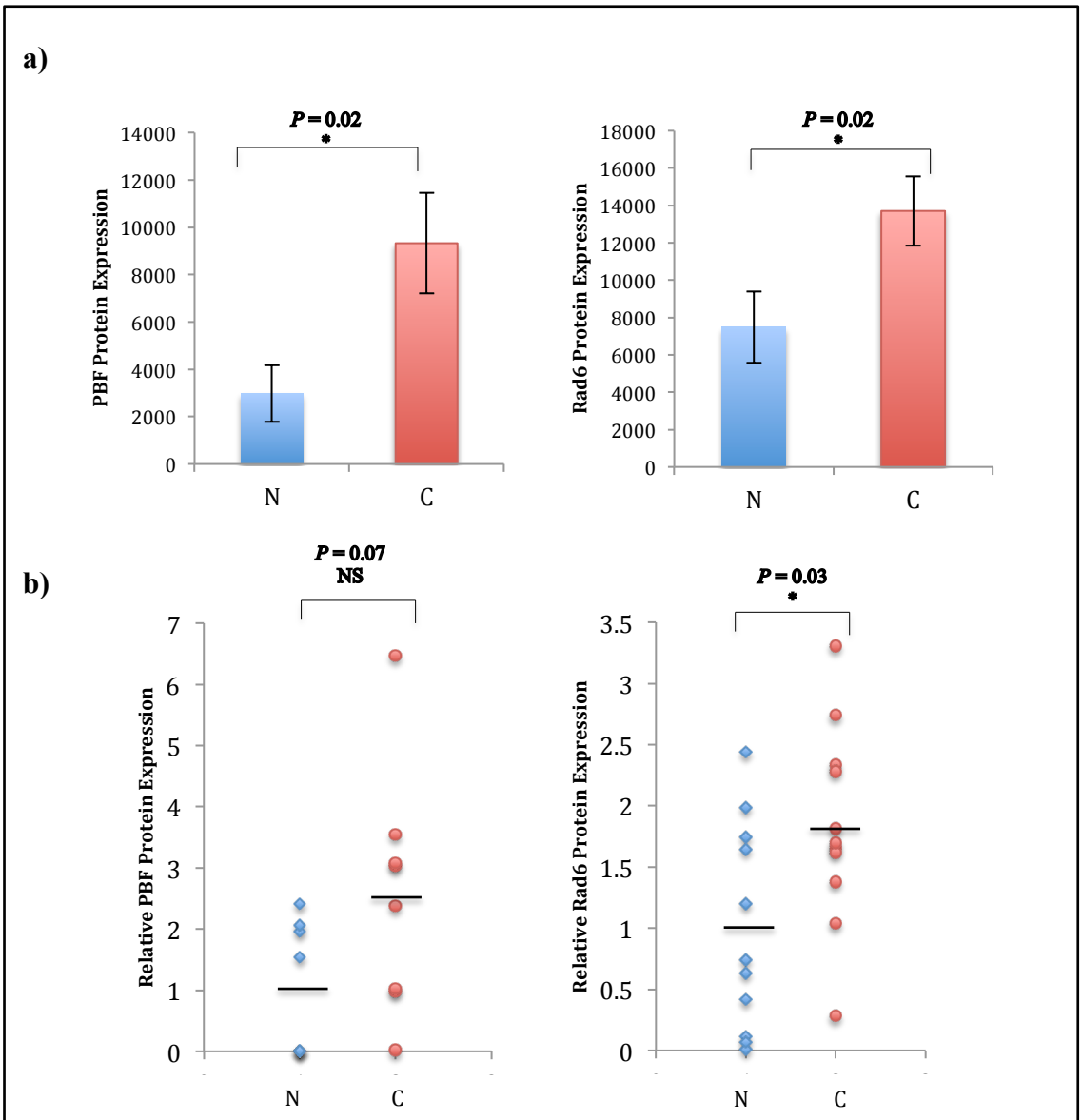

Figure 4.6: PBF and Rad6 Protein Expression in Normal and Cancerous Thyroids

Protein extracts from human matched normal and thyroid tumour pairs were analysed by western blotting. a) The intensities of PBF (n=9) and Rad6 (n=11) were then quantified and the expression relative to normal thyroid are shown. Data presented as mean ± SEM. b) Quantification of PBF (n=8) and Rad6 (n=10) protein expression relative to normal thyroid. Data presented as a scatter plot. NS: non-significant.

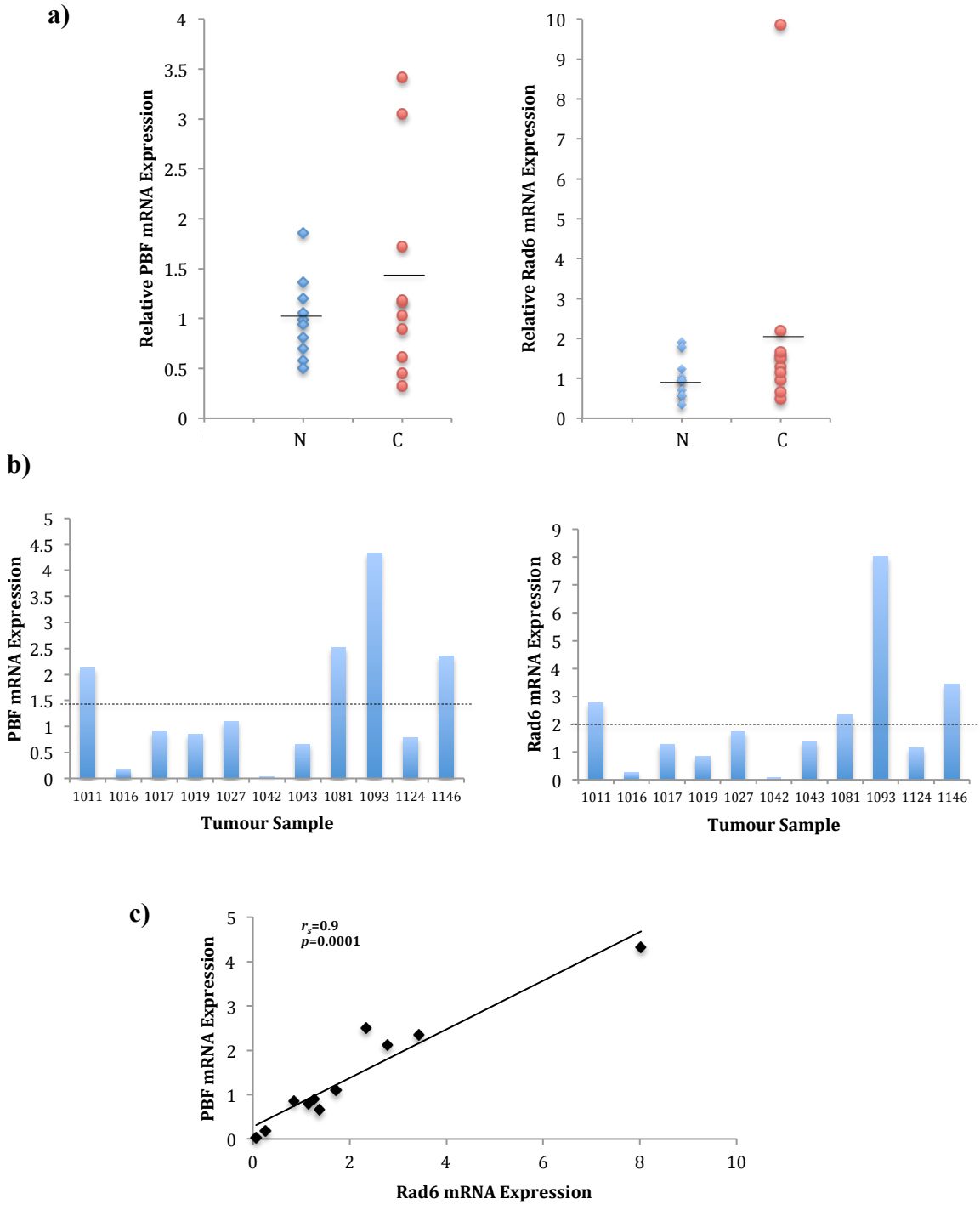

Figure 4.7: Correlation Between PBF and Rad6 mRNA Expression in Normal and Cancerous Thyroids

a) PBF and Rad6 mRNA expression was determined by Taqman RT-PCR of RNA extracted from matched normal and thyroid cancer pairs. Values were adjusted for 18S (housekeeping) gene expression and PBF (n=8) or Rad6 (n=10) mRNA expression in cancerous thyroids quantified relative to normal thyroid. Data presented as a scatter plot. b) Quantification of PBF and Rad6 mRNA expression in thyroid cancer relative to normal thyroid. Data presented as fold change in expression, (--): mean, n=11. c) Correlation of PBF and Rad6 mRNA expression (fold change) in cancerous and normal thyroids. Statistics analysed using Spearman rank correlation, n=11.

5. DISCUSSION

DNA damage checkpoints, that enable cell cycle arrest and repair of damaged DNA, are absolutely essential for the suppression of genome instability, one of the main driving forces behind tumour progression (53). The tumour suppressor, p53 is indispensible for the proper control of cellular responses towards DNA damage (68) and, as such, is typically regarded as the 'guardian of the genome'. Mutations in p53 are frequently observed in human cancer (48). Alterations in the post-translational modification of p53 through mutation or overexpression of key regulators, such as MDM2, are also implicated in the abrogation of p53 function in cancerous cells (69).

PBF has only been described in 16 publications to date and although it is ubiquitously expressed, its function remains elusive. Previous work has revealed PBF to be a proto-oncogene. It has been demonstrated to be overexpressed in thyroid (56,57,59), breast (58) and colorectal (54) cancer and is both transforming (*in vitro*) and tumourigenic (*in vivo*) (56). In addition, PBF has recently been identified as a novel regulator of p53 stability and function, with which it physically interacts (54). Oncogenic levels of PBF induced the polyubiquitination and subsequent degradation of p53(54). Furthermore, interaction with PBF prevented p53-mediated transactivation of downstream effectors, such as p21(54).

Rad6, an E2 ubiquitin ligase has also been implicated in the regulation of p53 (51-53) and has been identified as an interacting partner(51,52). Previous findings suggest that Rad6 is overexpressed in breast(67) and colorectal cancer(54). Furthermore, expression appears to be induced by overexpression of PBF (54). My current data now provides evidence of a potential role for Rad6 in PBF-mediated regulation of p53 in the papillary thyroid cancer cell lines, K1 and TPC-1.

Knockdown of Rad6 led to the induction of PBF and p53 expression in K1 cells. Conversely, Rad6 overexpression resulted in a reduction in p53 protein expression as well as PBF, although modest. Similar results were observed in TPC-1 cells. These findings are in accord with previous data demonstrating that Rad6 negatively regulates p53(52). Depletion of Rad6 resulted in the accumulation of p53, whereas overexpression led to rapid p53 ubiquitination and degradation(52). Of note, these experiments were performed in *Drosophila* S2 cells and, thus, may not reflect what is happening in mammalian cells. They must therefore be interpreted with caution. Indeed, *Drosophila* p53 (DMP53) and mammalian p53 are thought to be differentially regulated, as no MDM2 or p19ARF homologs have yet been uncovered in *D.melanogaster*(52).

The effect of Rad6 on p53 protein levels has recently been explored, by Chen *et al*, through depletion and overexpression of Rad6 in mammalian cells. Interestingly, alteration of Rad6 expression had no effect on p53 protein levels (53). A possible reason for the discrepancy could be that the papillary thyroid cancer cell lines potentially harbour mutations in the Rad6 gene resulting in altered protein function. Alternatively, abrogation of proteins involved in Rad6 or p53 regulation may also affect p53 expression. MDM2, for example, has been reported to accumulate in the nuclei of certain classes of differentiated papillary thyroid cancer(70) and is required for Rad6-mediated p53 degradation(51). Evidence suggests that Rad6 mediates the monoubiquitination of p53, whereas, further extension of the ubiquitin chain requires the presence of MDM2 in complex with Rad6 and p53(51). In this instance, overexpression of Rad6, coupled with aberrant MDM2 expression or accumulation, could result in the polyubiquitination and subsequent degradation of p53. Although the number of replicates was limited, when taken together, these results suggest that a

more complex relationship exists between PBF and Rad6 in the regulation of p53. Further repeats would be required to confirm these findings.

To further investigate the association between Rad6, PBF and p53, co-immunoprecipitation assays were performed. Both PBF and Rad6 have been shown to independently interact with p53 (51,54). Co-immunoprecipitation for p53 confirmed that Rad6 and p53 do indeed physically interact. Furthermore, co-immunoprecipitation for PBF identified Rad6 as a novel interacting partner. Unfortunately, due to time constraints, the functional consequence(s) of such an interaction was not explored. Rad6 binding to PBF may be required for the recruitment of MDM2, which, as mentioned above, is required for efficient p53 degradation. This is supported by preliminary findings that PBF directly interacts with MDM2 (Andy Turnell, unpublished data). It is well known that PTTG1 binds to PBF at the C-terminal region, which contains the NLS motif (55). This interaction is required for the nuclear localisation of PTTG1(55). Similarly, Rad6 binding to PBF maybe localised to this C-terminal region and may facilitate nuclear localisation of Rad6. Once in the nucleus, Rad6 may then alter p53 transcription through modifications to local chromatin, as has been previously described (figure 5.1) (53). Although the regions of Rad6 and PBF that are involved in the interaction remain to be determined, the data described represents the first study to report an *in vitro* association between Rad6 and PBF.

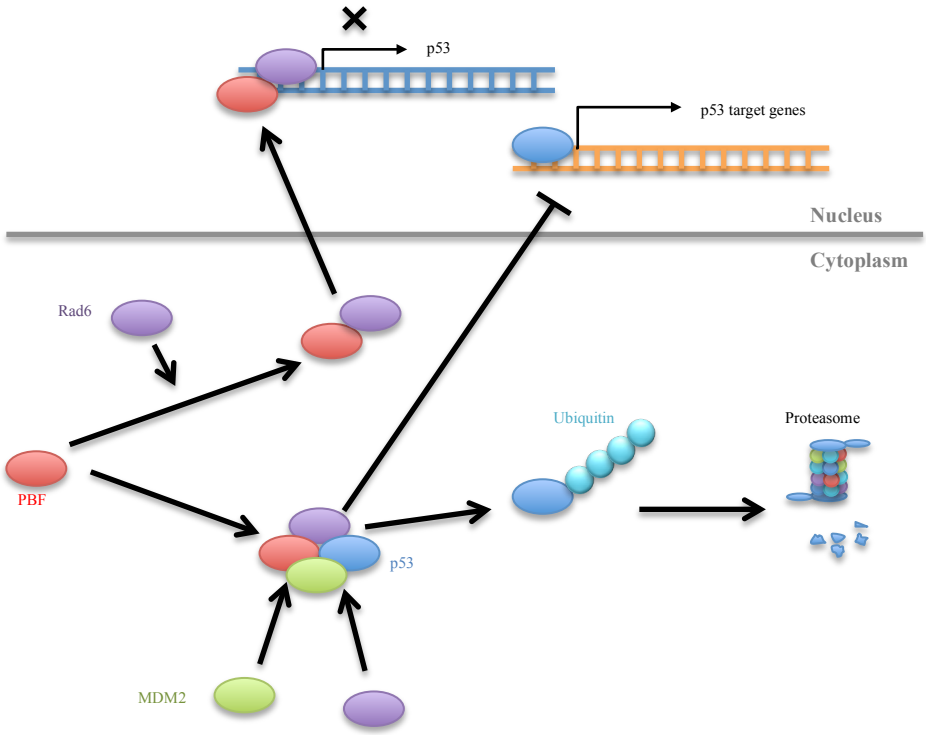

Figure 5.1: Proposed Model of PBF Regulation of p53 Stability and Function via Rad6

PBF binds to p53, possibly along with other binding partners such as Rad6 and MDM2, and induces the ubiquitination and degradation of p53 protein, thereby preventing transcription of p53 target genes. PBF may also facilitate the nuclear transport of Rad6, thus enabling Rad6-mediated modifications to local chromatin leading to altered p53 transcription.

It has previously been shown that PBF protein and mRNA levels are upregulated in thyroid cancer compared to normal thyroids(57), however Rad6 expression has never been explored, alongside PBF, in the thyroid. In this study, expression of Rad6 and PBF were found to be significantly altered in human thyroid tumours compared to matched normal tissues. Protein expression of Rad6 and PBF was elevated in the majority of tumours compared to matched normals. A similar trend was also observed for mRNA expression, although some differences between protein and mRNA expression were noted in the same samples. This discrepancy may be due to technical difficulties associated with RNA extraction from tissue samples, or could be a result of RNA degradation post-extraction. Interestingly, Rad6 mRNA expression was positively correlated with PBF mRNA expression, providing further support for our

earlier *in vitro* observations. This positive correlation has also been documented in colorectal tumours(54). Of note, protein expression in these samples was not normalised to β-actin. If time had permitted, the PVDF membranes would have been probed for another housekeeping gene, such as GAPDH.

In summary, the data outlined in this report provides evidence that the proto-oncogene PBF directly binds Rad6 and may regulate p53 function via this interaction. It also shows for the first time that Rad6 overexpression is frequent in thyroid cancer and that its expression appears to correlate with PBF expression. Taken together, these observations have important implications, not only in our understanding of cancer biology and pathogenesis, but also in the use of oncogenes and tumour suppressors as prognostic indicators.

5.1. Future Work

First and foremost, further characterisation of the apparent complex relationship between Rad6, PBF and p53 is required. Firstly, repeat experiments would need to be performed to confirm the effect of Rad6 expression on PBF and p53 expression in K1 and TPC-1 cells. PBF knockdown and overexpression should also be carried out to assess the influence of PBF on Rad6 and p53 expression.

Secondly, reciprocal co-immunoprecipitation experiments, where endogenous PBF is co-immunoprecipitated with an anti-Rad6 antibody, are needed to further prove binding of PBF with Rad6. In addition, GST pull-down assays using PBF and/or Rad6 mutants will facilitate in determining which regions are involved in binding.

Further protein and mRNA expression data is required, preferably using a larger number of matched normal and cancerous thyroid pairs. Sequencing of the p53 gene in these samples would also prove useful and would allow for comparison of p53 status with protein expression. Furthermore, if clinical details for each patient sample were available, Rad6 protein expression could be correlated with clinical outcome, thus providing information on the potential use of Rad6 expression as a prognostic indicator in thyroid cancer. Immunohistochemical analysis of formalin-fixed paraffin embedded human thyroid tumour specimens for Rad6, p53 and PBF would provide additional information on expression of these proteins, including their localisation.

6. REFERENCES

(40) Hunt PJ, Wass JAH. Thyroid Disease. eLS 2001.

(41) Thyroid Cancer Statistics-Key Facts. 2012; Available at: http://info.cancerresearchuk.org/cancerstats/keyfacts/thyroid-cancer/. Accessed August, 07, 2012.

(42) Grodski S, Brown T, Sidhu S, Gill A, Robinson B, Learoyd D, et al. Increasing incidence of thyroid cancer is due to increased pathologic detection. Surgery 2008;144(6):1038-1043.

(43) Thyroid Cancer-UK Incidence Statistics. 2012; Available at: http://info.cancerresearchuk.org/cancerstats/types/thyroid/incidence/#trends. Accessed August/07, 2012.

(44) Smallridge RC, Marlow LA, Copland JA. Anaplastic thyroid cancer: molecular pathogenesis and emerging therapies. Endocr Relat Cancer 2009;16(1):17-44.

(45) Mazzaferri EL, Kloos RT. Current approaches to primary therapy for papillary and follicular thyroid cancer. Journal of Clinical Endocrinology & Metabolism 2001;86(4):1447-1463.

(46) Kim D, Pemberton H, Stratford AL, Buelaert K, Watkinson JC, Lopes V, et al. Pituitary tumour transforming gene (PTTG) induces genetic instability in thyroid cells. Oncogene 2005;24(30):4861-4866.

(47) Levine AJ, Oren M. The first 30 years of p53: growing ever more complex. Nature Reviews Cancer 2009;9(10):749-758.

(48) Vogelstein B, Lane D, Levine AJ. Surfing the p53 network. Nature 2000;408(6810):307.

(49) Zedenius J, Larsson C, WALLIN G, BÄCKDAHL M, Aspenblad U, HÖÖG A, et al. Alterations of p53 and expression of WAF1/p21 in human thyroid tumors. Thyroid 1996;6(1):1-9.

(50) Malaguarnera R, Vella V, Vigneri R, Frasca F. p53 family proteins in thyroid cancer. Endocr Relat Cancer 2007;14(1):43-60.

(51) Lyakhovich A, Shekhar MPV. Supramolecular complex formation between Rad6 and proteins of the p53 pathway during DNA damage-induced response. Mol Cell Biol 2003;23(7):2463-2475.

(52) Chen S, Wei HM, Lv WW, Wang DL, Sun FL. E2 ligase dRad6 regulates DmP53 turnover in Drosophila. J Biol Chem 2011;286(11):9020.

(53) Chen S, Wang DL, Liu Y, Zhao L, Sun FL. RAD6 Regulates the Dosage of p53 by a Combination of Transcriptional and Posttranscriptional Mechanisms. Mol Cell Biol 2012;32(2):576-587.

(54) Read ML, Seed RI, Sharma N, Fong JCW, Kwan P, Smith VE, et al. The PTTG1-Binding Factor (PBF/PTTG1IP) Acts as a Novel Regulator of p53 Stability and Function in Human Cancers. Submitted to Cancer Research 2012.

(55) Chien W, Pei L. A novel binding factor facilitates nuclear translocation and transcriptional activation function of the pituitary tumor-transforming gene product. J Biol Chem 2000;275(25):19422-19427.

(56) Read ML, Lewy GD, Fong JCW, Sharma N, Seed RI, Smith VE, et al. Proto-oncogene PBF/PTTG1IP regulates thyroid cell growth and represses radioiodide treatment. Cancer Res 2011;71(19):6153-6164.

(57) Stratford AL, Boelaert K, Tannahill LA, Kim DS, Warfield A, Eggo MC, et al. Pituitary tumor transforming gene binding factor: a novel transforming gene in thyroid tumorigenesis. Journal of Clinical Endocrinology & Metabolism 2005;90(7):4341-4349.

(58) Watkins RJ, Read ML, Smith VE, Sharma N, Reynolds GM, Buckley L, et al. Pituitary tumor transforming gene binding factor: a new gene in breast cancer. Cancer Res 2010;70(9):3739.

(59) Hsueh C, Lin J, Chang Y, Hsueh S, Chao T, Yu J, et al. Prognostic Significance of Expression of Pituitary Tumour-Transforming Gene-Binding Factor in Papillary Thyroid Carcinoma. Under review - Clinical Endocrinology 2012.

(60) Boelaert K, Smith V, Stratford A, Kogai T, Tannahill L, Watkinson J, et al. PTTG and PBF repress the human sodium iodide symporter. Oncogene 2007;26(30):4344-4356.

(61) Smith VE, Read ML, Turnell AS, Watkins RJ, Watkinson JC, Lewy GD, et al. A novel mechanism of sodium iodide symporter repression in differentiated thyroid cancer. J Cell Sci 2009;122(18):3393-3402.

(62) Smith VE, Franklyn JA, McCabe CJ. Expression and function of the novel proto-oncogene PBF in thyroid cancer: a new target for augmenting radioiodine uptake. Journal of Endocrinology 2011 August 01;210(2):157-163.

(63) Koken M, Reynolds P, Jaspers-Dekker I, Prakash L, Prakash S, Bootsma D, et al. Structural and functional conservation of two human homologs of the yeast DNA repair gene RAD6. Proceedings of the National Academy of Sciences 1991;88(20):8865.

(64) Enserink JM, Kolodner RD. What makes the engine hum: Rad6, a cell cycle supercharger. Cell Cycle 2012 Jan 15;11(2):249-252.

(65) Zimmermann C, Chymkowitch P, Eldholm V, Putnam CD, Lindvall JM, Omerzu M, et al. A chemical-genetic screen to unravel the genetic network of CDC28/CDK1 links ubiquitin and Rad6–Bre1 to cell cycle progression. Proceedings of the National Academy of Sciences 2011;108(46):18748-18753.

(66) Giannattasio M, Lazzaro F, Plevani P, Muzi-Falconi M. The DNA damage checkpoint response requires histone H2B ubiquitination by Rad6-Bre1 and H3 methylation by Dot1. J Biol Chem 2005;280(11):9879-9886.

(67) Shekhar MPV, Lyakhovich A, Visscher DW, Heng H, Kondrat N. Rad6 overexpression induces multinucleation, centrosome amplification, abnormal mitosis, aneuploidy, and transformation. Cancer Res 2002;62(7):2115.

(68) Wahl GM, Carr AM. The evolution of diverse biological responses to DNA damage: insights from yeast and p53. Nat Cell Biol 2001;3(12):277-277.

(69) Momand J, Wu HH, Dasgupta G. MDM2—master regulator of the p53 tumor suppressor protein. Gene 2000;242(1):15-29.

(70) Jennings T, Bratslavsky G, Gerasimov G, Troshina K, Bronstein M, Dedov I, et al. Nuclear accumulation of MDM2 protein in well-differentiated papillary thyroid carcinomas. Exp Mol Pathol 1995;62(3):199-206.